

On the collision of a droplet with a solid surface

BY S. CHANDRA† AND C. T. AVEDISIAN

Sibley School of Mechanical and Aerospace Engineering, Cornell University, Ithaca, New York 14853-7501, U.S.A.

The collision dynamics of a liquid droplet on a solid metallic surface were studied using a flash photographic method. The intent was to provide clear images of the droplet structure during the deformation process. The ambient pressure (0.101 MPa), surface material (polished stainless steel), initial droplet diameter (about 1.5 mm), liquid (n-heptane) and impact Weber number (43) were fixed. The primary parameter was the surface temperature, which ranged from 24 °C to above the Leidenfrost temperature of the liquid. Experiments were also performed on a droplet impacting a surface on which there existed a liquid film created by deposition of a prior droplet.

The evolution of wetted area and spreading rate, both of a droplet on a stainless steel surface and of a droplet spreading over a thin liquid film, were found to be independent of surface temperature during the early period of impact. This result was attributed to negligible surface tension and viscous effects, and in consequence the measurements made during the early period of the impact process were in good agreement with previously published analyses which neglected these effects. A single bubble was observed to form within the droplet during impact at low temperatures. As surface temperature was increased the population of bubbles within the droplet also increased because of progressive activation of nucleation sites on the stainless steel surface. At surface temperatures near to the boiling point of heptane, a spoke-like cellular structure in the liquid was created during the spreading process by coalescence of a ring of bubbles that had formed within the droplet. At higher temperatures, but below the Leidenfrost point, numerous bubbles appeared within the droplet, yet the overall droplet shape, particularly in the early stages of impact (< 0.8 ms), was unaffected by the presence of these bubbles. The maximum value of the diameter of liquid which spreads on the surface is shown to agree with predictions from a simplified model.

Nomenclature

A	Hamaker constant
c	heat capacity
d	diameter of the liquid film
d_{\max}	maximum extension diameter of the liquid film
D	initial droplet diameter
h	height of the liquid film above the solid surface

† Present address: Department of Mechanical Engineering, University of Toronto, Toronto, Ontario, Canada M5S 1A4.

h_{ig}	latent heat of evaporation
k	thermal conductivity
E_K	kinetic energy
E_S	surface energy
P_σ	interfacial tension pressure
P_s	stagnation pressure
Re	Reynolds number ($\equiv \rho UD/\mu$)
r	radius of surface cavity opening
r_i	radius of curvature of the liquid at the tip of the spreading liquid film
t	time
t_c	time taken for the droplet height to go from its maximum value of D to 0
t_e	droplet evaporation time
t_r	residence time of the droplet on the surface (time at which $\beta \rightarrow 0$)
T	temperature
T_C	critical temperature
T_L	temperature of the liquid
T_{Leid}	Leidenfrost temperature
T_b	boiling point of the liquid
T_w	temperature of the solid surface
T_∞	ambient temperature
U	droplet impact velocity
v	velocity component
V	droplet volume
W	energy lost in deforming the drop against viscosity
We	Weber number ($\equiv \rho U^2 D/\sigma$)
α	angle of inclination of the camera to the horizontal
β	$\equiv d/D$
Γ	mass flow rate of liquid into the meniscus
δ	film thickness
Δ	ratio of the stagnation pressure force to the surface tension force
ζ	$\equiv h/D$
θ	'apparent' advancing liquid–solid contact angle at the contact line
κ	$\equiv 1/(kpc)$
μ	viscosity
ν	kinematic viscosity
ρ	density
σ	surface tension
τ	viscous shear stress
ϕ	dissipation function
Ψ	ratio of the stagnation pressure force to the viscous force

1. Introduction

The problem of isolated droplets impacting surfaces has been studied since the time of Worthington (1877*a, b*, 1908), and it is still currently of interest in such applications as fire suppression via sprinkler systems, impingement of liquid droplets on gas turbine engine blades by in-flight rain ingestion, cooling of electronic equipment by a liquid spray or droplet stream, and combustion of sprays in confined

geometries (e.g. spray-fired incinerators and automotive engines). Relevant droplet sizes range from micrometres (e.g. spray combustion applications) to millimetres (e.g. fire extinguishment and rain ingestion within gas turbine engines).

In these applications a liquid droplet travels through a gas and terminates its flight by colliding with a solid surface. When the droplet hits the surface it can splash, spread, and/or rebound. The scenario to be expected depends on both the impact energy of the droplet and the temperature of the surface. For high impact energy, a measure of which is the Weber number ($We \equiv \rho U^2 D / \sigma$), the droplet may shatter during the deformation process, whereas for low Weber numbers the droplet may stick and spread and ultimately reside as a lens-shaped mass on the surface, or rebound from the surface. Previous photographic studies of the impact process have examined the droplet impact dynamics with the impact energy as the parameter. The present work examines the effect of surface temperature on the impact dynamics with the initial impact energy fixed.

The liquid studied was n-heptane (C_7H_{16}) because of its relevance as a model hydrocarbon fuel; dynamic information of heptane droplet impact on surfaces will be qualitatively similar to that of other liquids (e.g. water). The droplet velocity at the time of impact was 0.93 m s^{-1} . The Weber number was 43 and the impact Reynolds number ($Re = \rho U D / \mu$) was 2300.

The principal parameter was the surface temperature, which was varied from 24°C to 250°C . This temperature range encompassed the liquid boiling point (98.4°C) and the Leidenfrost point for heptane. The initial droplet diameter (1.50 mm), ambient pressure (0.101 MPa), ambient temperature (*ca.* 22°C), and test surface material (polished stainless steel surface) were held constant to isolate the effect of surface temperature.

For fixed droplet impact energy, the surface temperature can effect the impact dynamics. As the droplet approaches the surface it evaporates because of heat transfer between the surface and the droplet. The vapours generated between the droplet and surface are compressed as the droplet moves closer to the surface. At sufficiently high surface temperature (i.e. above the liquid's Leidenfrost temperature) the droplet evaporates fast enough that this compression can result in a gas pressure between the droplet and surface which can provide a braking action to the droplet sufficient to not only slow the droplet but prevent droplet/surface contact. The dynamics of impact will then be different than at low temperature where the momentum of the droplet may be sufficient to overcome the effect of compression.

Central to a fundamental understanding of the dynamics of impact on a solid surface is the ability to record the progressive stages of deformation of the droplet as it is crushed during impact. This fact requires the ability to essentially freeze the droplet's image at various stages during impact. A variety of high-speed ciné film, and short-duration single-shot photographic techniques have been used to this end (see, for example, Worthington 1908; Savic & Boulton 1955; Wachters & Westerling 1966; Toda 1974; Akao *et al.* 1980; Inada *et al.* 1983). The method which has yielded the greatest clarity is single-shot flash photography. The earliest of such techniques exposed the film by the light produced by spark discharge of a capacitor (Worthington 1977*a, b*, 1908). The subsequent development of modern electronic flash (Edgerton 1979) and laser equipment made it possible to more reliably trigger the flash and with a more controlled light intensity and duration.

Wachters & Westerling (1966) used such a method to study water droplets impacting a stainless steel surface maintained at a temperature of 400°C . The

parameter was the Weber number. Similar experiments were carried out by Akao *et al.* (1980), but the photographs did not reproduce as well. High-speed ciné photography has also been used to record the impact dynamics of droplets with some reduction in image quality (Engel 1955; Brunton & Camus 1970; Savic & Boulton 1955; Savic 1958; Toda 1974; Inada *et al.* 1983).

The quality of the photographs of the droplet impact process published in the past has not been sufficient to clearly discern phenomena occurring within the drop, such as for example, bubble formation. The key is to be able to diffuse the light sufficiently to wash out reflections of light within the droplet, while at the same time maintaining a sufficient depth of field, magnification, and short enough exposure time to reduce image blurring. The work reported here describes a single-shot flash photographic technique which accomplishes these objectives for the case of droplets impacting with no tangential velocity (i.e. normal impact).

In a single-shot method only one image is taken at one instant during the impact process for each drop studied. The assumption is that the impact process is sufficiently repeatable from drop to drop that by photographing successive stages of the impact of several different drops (one image per drop) the evolution of the droplet dynamics can be pieced together from initial images of droplets taken at progressive stages during impact. Such is true for droplets impacting surfaces.

The objectives of this study were to (1) photograph the impact of a droplet on a surface whose temperature was varied from room temperature to above the Leidenfrost point of the liquid, (2) measure the evolution of droplet shape during impact (e.g. spreading diameter and droplet height), and (3) compare the results with relevant analyses.

2. Description of the experimental apparatus

Figure 1 is a schematic diagram of the experimental apparatus. The main components are (1) a syringe pump and hypodermic needle to form and release the drop, (2) a flat stainless steel surface on which the droplet fell, (3) a 35 mm camera, (4) a flash unit to provide illumination for photography, and (5) an optical interrupter and time delay circuit to detect the release of the droplet and trigger the flash.

A droplet was formed by forcing liquid from a Sage Instruments model 341A syringe pump at a flow rate of 0.69 ml min^{-1} through a stainless steel hypodermic needle. The needle was flat tipped, with an outer diameter of 0.20 mm and an inner diameter of 0.15 mm. The flow rate was low enough to allow a droplet to form at the needle tip and detach under its own weight. To ensure repeatability of droplet formation and release it was necessary to ensure that the liquid remained free of any air bubbles. To keep the outside of the needle free from any dust particles it was periodically wiped clean with a cotton swab soaked in n-heptane. It was essential to minimize any vibrations that the apparatus may experience during droplet detachment; experiments were therefore conducted at night when vibrations in the laboratory building were at their lowest.

The needle was placed with its tip located 45 mm above the test surface. At this height the kinetic energy of the droplet at the instant of impact with the surface was not sufficient to shatter or break up the droplet when the surface was at room temperature. The droplet fell onto a 12.7 mm thick by 76.2 mm diameter stainless steel test surface. The surface was polished using 600 grit energy cloth, and then

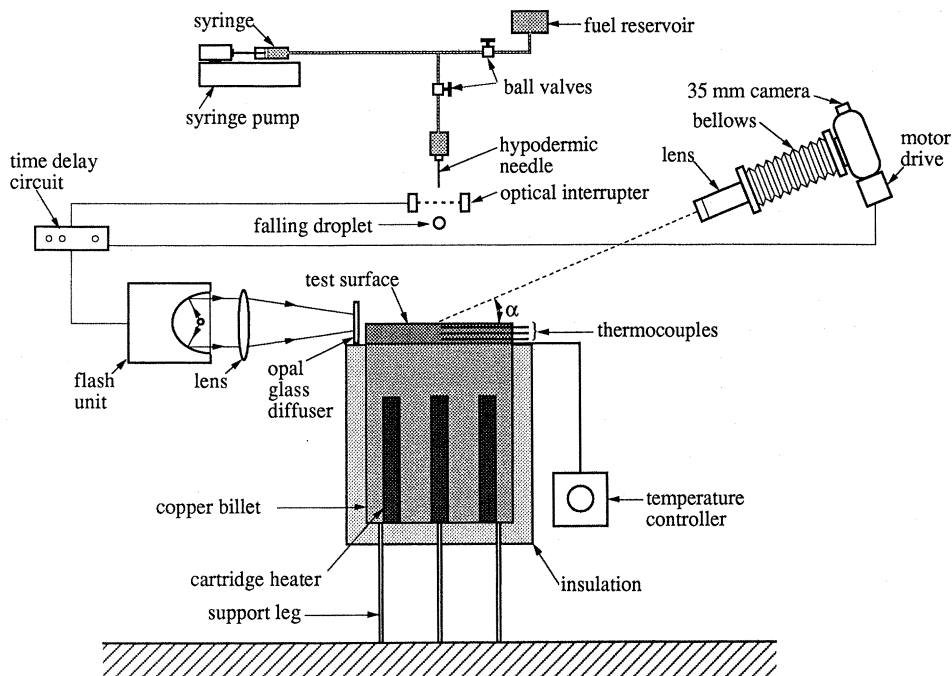


Figure 1. Schematic of the apparatus.

brought to a mirror finish with Wenol metal polish. The surface was heated by placing it on a cylindrical copper billet containing five symmetrically placed cartridge heaters (Hotwatt HS374). The surface temperature could be controlled accurate to $\pm 1^\circ\text{C}$ using an Omega E924K analogue temperature controller. The test surface temperature was measured by extrapolating the measurements of three 1 mm diameter stainless steel sheathed chromel–alumel thermocouples (Omega SCASS-040G-6) inserted into the surface as shown in figure 1. Extrapolated surface temperatures were found to be within 1°C of the temperature recorded by the uppermost thermocouple (located 0.8 mm below the centre of the upper surface).

The release of the droplet was detected by placing an optical interrupter (G.E. H21B1) approximately 5 mm below the tip of the needle. The optical interrupter was a single unit housing both a light emitting diode and a photo-transistor with a separation gap of 3 mm. The passage of a drop through this gap interrupted the light beam and sent a signal to a time delay unit which opened the camera shutter. After a preset time interval the flash unit was triggered. The time delay circuit consisted of a 1 MHz oscillator and a 20 bit binary counter. The required time delay (in microseconds) was loaded into the counter which was decremented on each oscilloscope pulse after the droplet passed through the optical interrupter. Once the counter reached zero, the flash was triggered. The time delay between the light beam interruption and flash triggering could be set with a resolution of $1\ \mu\text{s}$. Further details of the electronics are described elsewhere (Chandra 1990).

Two means for illumination were used: (1) an E.G.&G. 549-11 flash unit that provided a $0.5\ \mu\text{s}$ duration flash, and (2) a General Radio 1538A strobe combined with a 1538P4 high intensity flash capacitor which provided an $8\ \mu\text{s}$ flash. The longer period of illumination allowed lower speed film to be used and improved the

resolution of the photographs. No significant blurring of the image could be seen due to the longer exposure time.

Lighting was provided by directing the light from the flash onto a Fresnel lens (Ealing 34-7682) 152.4 mm in diameter and with a focal length of 76.2 mm. The lens was placed 15 mm in front of the flash unit. The light was focused by the lens onto a 50 mm opal glass diffuser (Ealing 26-6528) which was positioned along the same axis as the lens 65 mm in front of it. The diffuser was placed 10 mm from the site of the droplet impact. The axis of the flash, lens, and diffuser was in the same plane as the surface on which the droplet impacted (*cf.* figure 1).

Photographs were taken using a Nikon F-3 camera equipped with a 105 mm f-4 lens, extension bellows (Nikon PB-6 combined with PB-6E), and motor drive (MD-4). The camera was aligned at an angle α to the horizontal where α was set equal to either 0° , 30° or 60° . The front of the camera lens was placed 90 mm from the droplet and the bellows were extended to 390 mm to give a magnification of approximately 4. The lens aperture was stopped down to f-22 to provide adequate depth of field. Upon release of the droplet the time delay circuit opened the camera shutter for $\frac{1}{8}$ s, during which period the flash was triggered. The intensity of the flash was so much greater than that of the ambient light that the film was effectively exposed only by the light of the flash even though the shutter was actually opened for a much longer period. The camera mirror was locked in the 'up' position while photographs were taken to minimize any vibrations.

The film used with the 0.5 μ s duration flash was Kodak TMAX 400. Film exposed with a very short duration flash tends to lose image contrast (Edgerton 1979). Therefore to enhance contrast the film was push processed to 1600 ASA by developing for 8 min in Kodak TMAX developer at 24°C . With the 8 ms duration flash Kodak TMAX 100 film was used and push processed to 400 ASA in TMAX developer for 9 min at 24°C . Prints were made on Kodak Polycontrast RC III paper using a no. 4 polycontrast filter.

Measurements of droplet dimensions were made directly from 35 mm negatives by placing the film in a photographic enlarger and projecting the image with a magnification of approximately 50. Dimensions were calibrated using a scale factor determined from a photograph of a 4.763 mm diameter stainless steel dowel. The resolution of measurements made from the projected image using dividers and a steel scale was ± 0.5 mm which translates into an accuracy of droplet diameter measurement of ± 0.01 mm.

Total droplet evaporation times were measured using a Video Logic CDR 460 video camera to which was attached a Nikon 105 mm lens and extension bellows (Nikon PB-6). Front lighting was furnished by a General Radio 1538A strobe that was driven by the camera. The strobe provided 1 μ s duration images at a rate of 30 per second, thus eliminating any blurring of the image. A time display with a resolution of 0.1 s was added to the video image by a Vicon V240TW timer. The droplet evaporation time was defined as the interval between droplet impact and the instant when the droplet could no longer be seen.

3. Discussion

3.1. *Experimental observations of impact dynamics*

Figure 2 is a sequence of photographs ($\alpha = 0$ in figure 1) showing the impact of a drop of n-heptane on a stainless steel surface at 24°C . The first 2.6 ms of impact is

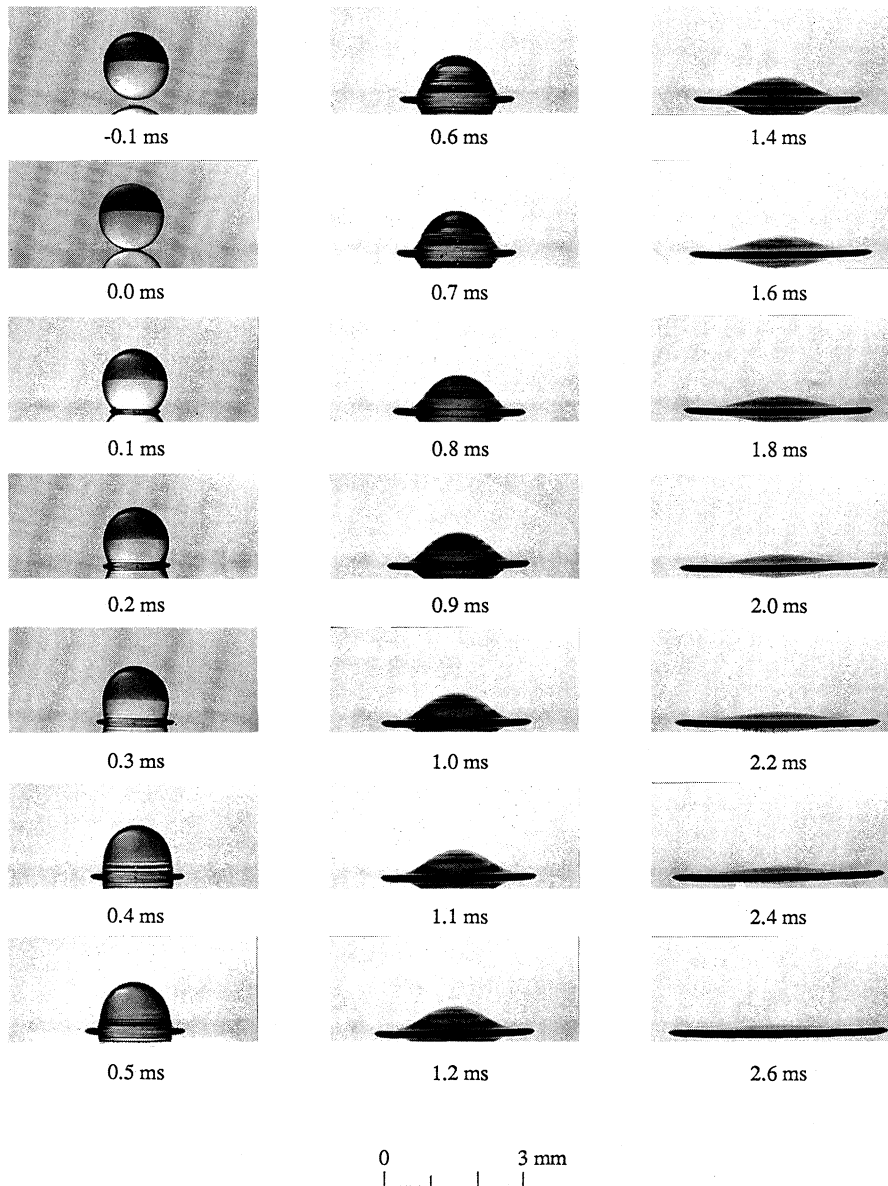


Figure 2. The impact of a n-heptane droplet on a stainless steel surface at 24 °C ($\alpha = 0^\circ$).

shown during which period the droplet assumed the shape of a flattened disc. The liquid continued to spread after this time, reaching a maximum diameter of 6.04 mm at approximately 20 ms after making contact with the surface. The upper half of the droplet appears to be darker than the lower half because the edge of the stainless steel surface is reflected in the droplet which acts as a convex lens inverting the image. The impact has two clearly visible effects on the droplet.

Firstly, liquid jets out sideways from beneath the droplet away from the point of impact. This jetting is observed to begin within the first 0.1 ms after contact with the surface. The sideways jetting of the liquid is caused by the rapid pressure increase in

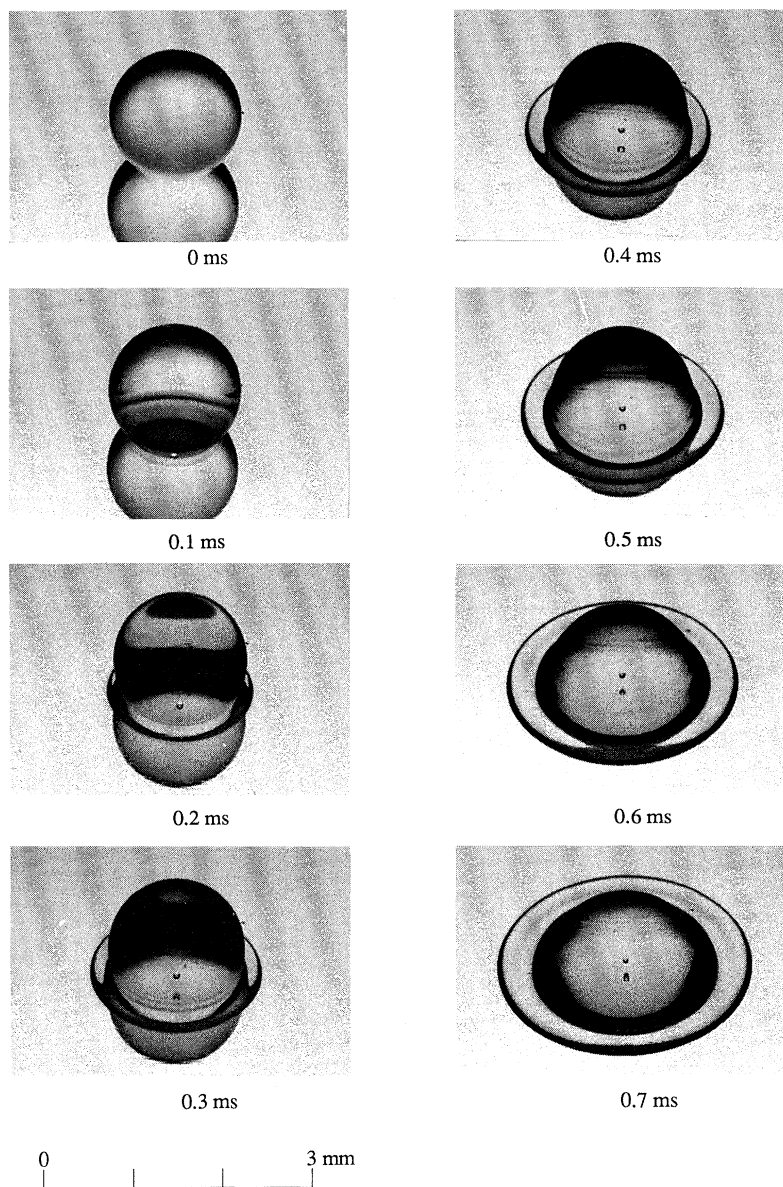


Figure 3. The impact of a n-heptane droplet on a stainless steel surface at 24 °C ($\alpha = 60^\circ$). A bubble can be seen to form at the point of impact.

the drop at the point of impact (Huang *et al.* 1973). The pressure is relieved by motion of the liquid along the surface in a 'film' that jets out ahead of the expanding base of the droplet (the structure of this film is discussed below). A second film or 'extended meniscus' may exist at the leading edge of this film. However, the thickness of the extended meniscus is typically on the order of 1 μm (Cook *et al.* 1981) and is therefore too small to be seen with the present optical set-up. It also may not have formed in the early times (on the order of milliseconds) that characterized the impact process.

Secondly, rings or waves around the periphery of the droplet can be seen (e.g. at $t = 0.4$ ms). These waves propagate away from the point of impact into the liquid. They could be caused by the compression of the liquid during impact. The dark rings that can also be seen inside the drop (e.g. $t = 0.8$ ms) may be caused by light refracted from the waves on the front and rear surfaces of the drop. Additional views at 24°C are shown in figure 3 taken at camera angle $\alpha = 60^\circ$. The dark rings are again visible early in the impact history (0.3 ms) but disappear as the impact proceeds.

Figure 3 clearly shows a single bubble inside the droplet. This bubble originated at the point of impact at $t = 1$ ms and then rose above the surface into the droplet as shown in figure 3. Two possible mechanisms for the formation of bubbles within a droplet which is at a temperature lower than its normal boiling point are (1) entrapment of air at the liquid–solid interface during impact, and (2) cavitation within the liquid caused by a lowering of the liquid pressure to below its saturation vapour pressure during the jetting process.

Air entrapment, leading to a bubble within the droplet, can occur by deformation of the liquid during the impact process. A bubble can be created in the liquid if a cusp or cavity, formed in the liquid during the impact process, ultimately becomes enclosed. The deformation can be in the liquid when a droplet impacts a solid surface or in the substrate when a liquid impacts another liquid (Yiantsios & David 1989; Longuet-Higgins 1990).

Cavitation – the process of bubble formation by isothermal decompression of a liquid (as distinct from the deformation mechanism mentioned above) – has also been offered as an explanation for the formation of bubbles inside an impacting drop for the case of a moving solid surface impacting a stationary pendant drop (Brunton & Camus 1970). The extreme case of homogeneous cavitation in which the pressure inside the droplet falls below the tensile strength of the liquid is unlikely to occur because of the presence of microscopic impurities in the drop. Two ways for the liquid pressure to be reduced are (Engel 1955; Huang & Hammitt 1972) (1) rapid radial jetting of the liquid along the droplet axis, and (2) propagation of compression waves away from the point of impact which reflect off the free surface of the droplet and return as expansion waves. The superposition of expansion and compression waves result in the formation of regions of low and high pressure. It was not possible to determine the mechanism (air entrapment or cavitation) for bubble formation from experiments involving droplets impacting solid surfaces.

Additional experiments were performed in which a droplet impacted a surface on which there was a pre-existing thin liquid film (which is relevant to liquid sprays or droplet streams impacting surfaces (Yao *et al.* 1988)). Figure 4 shows representative results. The liquid film was created by the spreading of another droplet of the same size which had fallen on the surface approximately 5 s earlier. A single bubble is again visible in the centre of the impacting drop (*cf.* $t = 0.2$ ms). Though the pre-existing liquid film appears to significantly alter the spreading of the droplet (compare figure 4 with figure 2), and the boundary conditions at the underside of the advancing liquid jet are definitely influenced by the pre-existing film at the surface, a bubble still forms. Sideways jetting of liquid is initiated at $t < 0.1$ ms as shown in figure 4. An annular ridge of liquid forms in the film (*cf.* $t = 0.9$ ms) and propagates radially outward. Ripples on the surface of the film propagate ahead of the ridge ($t = 1.5$ ms), and eventually both ripples and ridges disappear (*cf.* $t = 19.9$ ms in figure 4).

The conventional method of identifying the values of surface temperature at which changes occur in the impact, spreading, and evaporation process (e.g. a transition

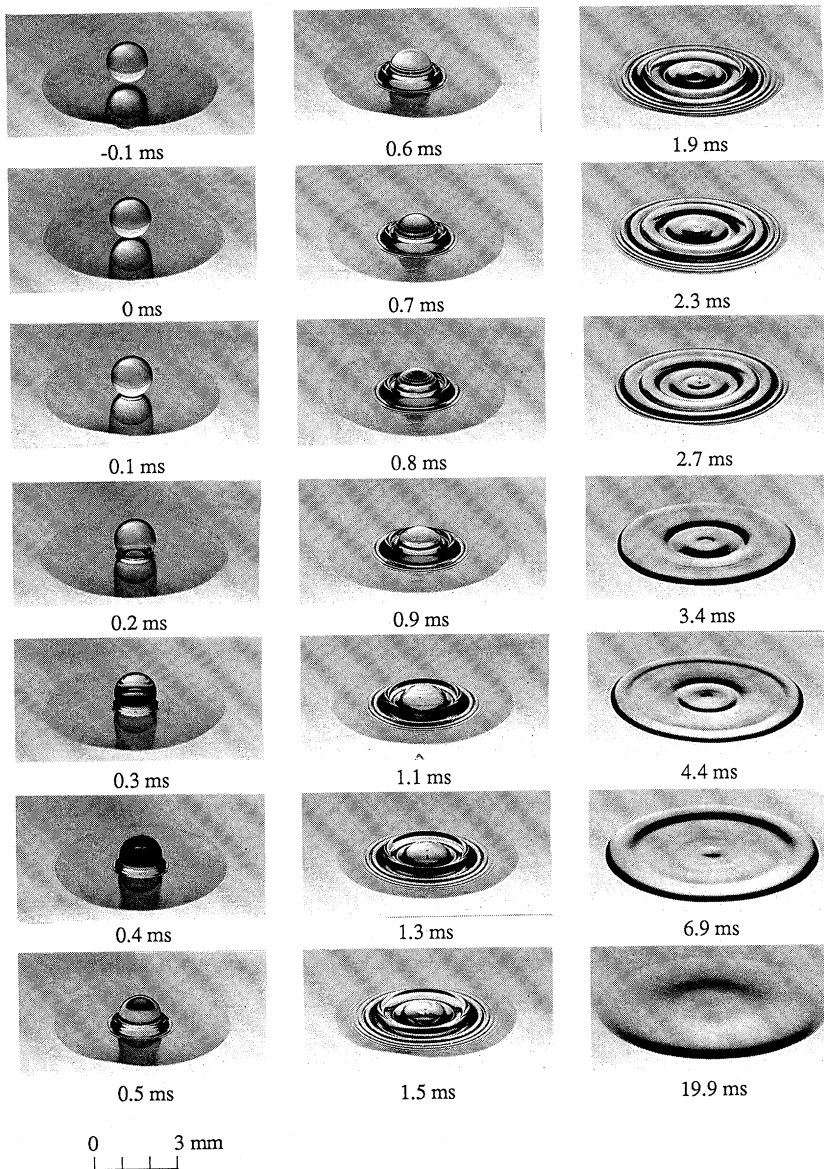


Figure 4. The impact of a n-heptane droplet on a thin liquid film on a stainless steel surface at 22 °C ($\alpha = 30^\circ$).

from nucleate to film boiling) has been to plot a curve of the droplet lifetime (t_e) as a function of the surface temperature (Baumeister & Simon 1973). Such a curve is shown in figure 5 for heptane.

As T_w is raised above the boiling point of n-heptane ($T_b = 98.4^\circ\text{C}$) bubbling occurs within the droplet by nucleate boiling of liquid in contact with the surface. The bubbles grow from surface imperfections in which liquid is trapped. An increasing number of surface nucleation sites are activated as temperature increases, and t_e decreases with increasing T_w . For $T_w \geq 180^\circ\text{C}$ the pressure of the vapour escaping from below the drop increases enough to levitate the droplet and the bulk liquid mass

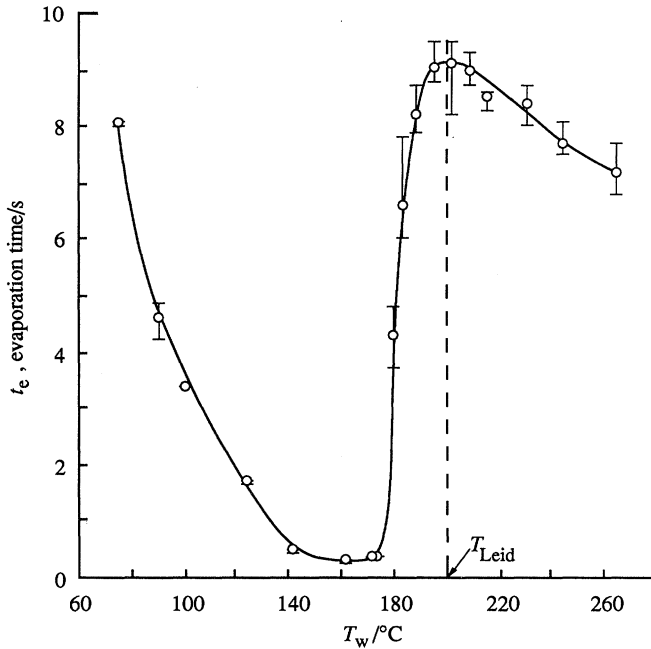


Figure 5. Leidenfrost curve for droplets of n-heptane (1.5 mm initial diameter) on a stainless steel surface.

makes only intermittent contact with the surface (Nishio & Hirata 1978). The evaporation time therefore starts increasing as T_w increases until for high enough T_w all liquid–solid contact ceases. The droplet is then in stable film boiling which is characterized by heat transfer to the droplet occurring by conduction across a thin film of vapour. For heptane this condition occurs at about 200 °C on a stainless steel surface. As T_w further increases beyond 200 °C, t_e begins to decrease due to increasing heat transfer across the vapour film. The surface temperature at which the droplet evaporation time is maximum is known as the Leidenfrost temperature (T_{Leid}).

Figure 6 depicts the impact and spreading process at several surface temperatures. The photographs were taken at $\alpha = 30^\circ$, which provides a perspective view that more clearly reveals the structure of the liquid film. The film thickness is not constant as a planar view might suggest (*cf.* figure 2). Rather, the liquid boundary alternatively decreases and increases. The varying film thickness may have been created by a hydraulic jump in the advancing liquid film, similar to the hydraulic jump that often occurs during normal impact of a laminar liquid jet on a flat surface. For low surface temperature (e.g. figure 6*a*) the spreading process also resembles the wave motion which are created when a stone splashes onto the free surface of a liquid pool.

At a surface temperature of 24 °C a single bubble can be seen at the centre of the drop (similar to that shown in figure 3) until $t = 6.2$ ms. The bubble disappears after this time, perhaps because it condensed due to the lack of any heat input which could have driven its further growth. At $T_w = 90$ °C (*cf.* figure 6*b*) and $T_w = 104$ °C (figure 6*c*) a similar bubble is seen at the centre of the drop ($t = 1.6$ ms). But at this temperature ten to fifteen additional bubbles are visible in a ring approximately 1 mm in diameter which surrounds the centre bubble (e.g. $t = 3.2$ ms). This bubble ring is less clearly visible when the surface temperature is 8 °C below the boiling point

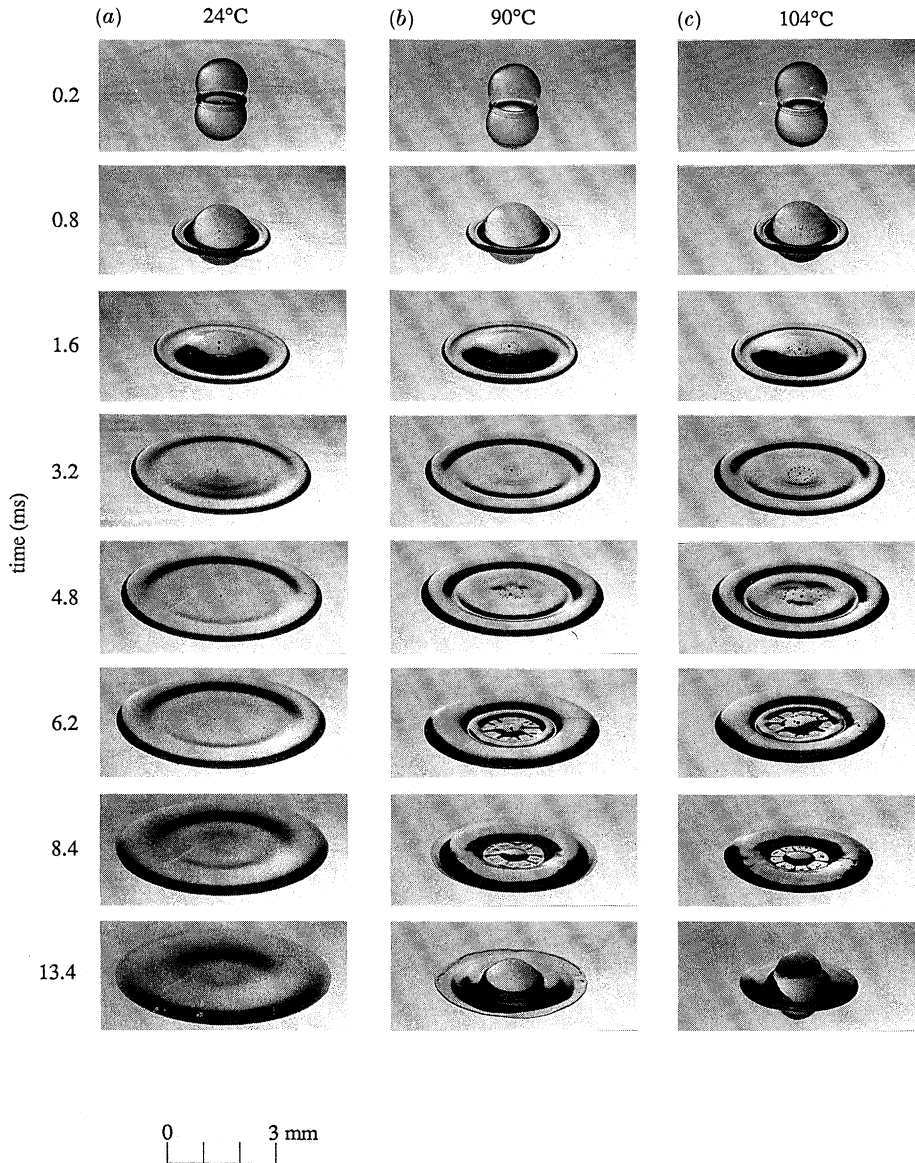


Figure 6. The impact of a n-heptane droplet on a heated stainless steel surface ($\alpha = 30^\circ$), with (a) $T_w = 24^\circ\text{C}$, (b) $T_w = 90^\circ\text{C}$, and (c) $T_w = 104^\circ\text{C}$.

as shown in figure 6*b*. The lowest surface temperature at which the bubble ring could be seen was $T_w = 80^\circ\text{C}$. The fact that the bubble ring appears only at high surface temperature and not at room temperature makes it unlikely that the ring is created by air entrapment between the surface and the droplet because the entrapment mechanism should not be strongly influenced by surface temperature. That the bubble ring is seen at temperatures below the boiling point suggests that it is caused by cavitation.

At $t = 6.2$ ms a number of circular and radial ridges can be seen on the surface of the liquid film at both $T_w = 90^\circ\text{C}$ and $T_w = 104^\circ\text{C}$, but not at $T_w = 24^\circ\text{C}$. The fact

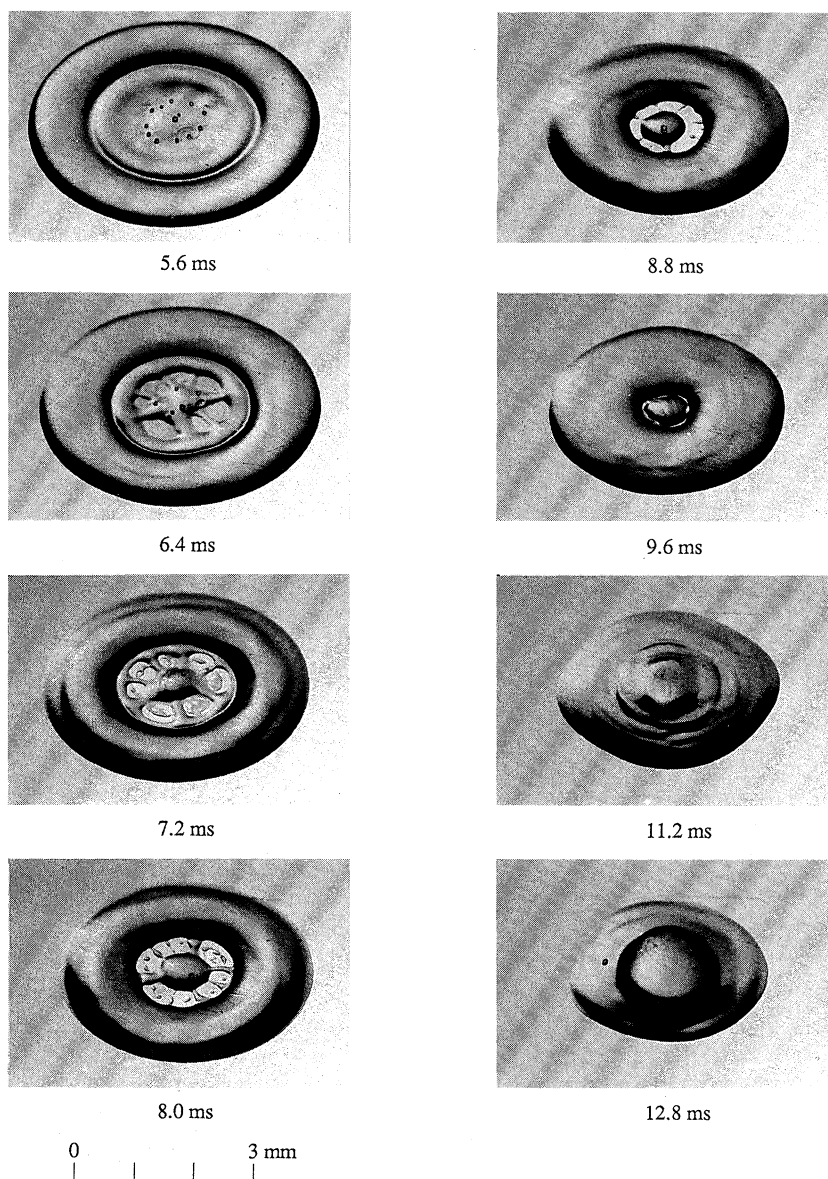


Figure 7. The formation of cellular structures in the liquid film during the spreading of a n-heptane droplet on a stainless steel surface at $104\text{ }^{\circ}\text{C}$ ($\alpha = 60^{\circ}$).

that these ridges are seen only at elevated surface temperatures implies that they may be created by temperature gradients within the liquid which, in turn, create surface tension gradients. Such surface tension driven convection in a thin liquid film may lead to the formation of cells of recirculating liquid (Block 1956) such as those observed here (e.g. $T_w = 104\text{ }^{\circ}\text{C}$, $t = 6.2\text{ ms}$ in figure 6*b* and *c*).

Details of the formation of the ridge and cellular structures at $T_w = 104\text{ }^{\circ}\text{C}$ are shown in figure 7. The photographs were taken with $\alpha = 60^{\circ}$ to obtain a better view of structures within the drop. At 5.6 ms after impact the ring of cavitation bubbles

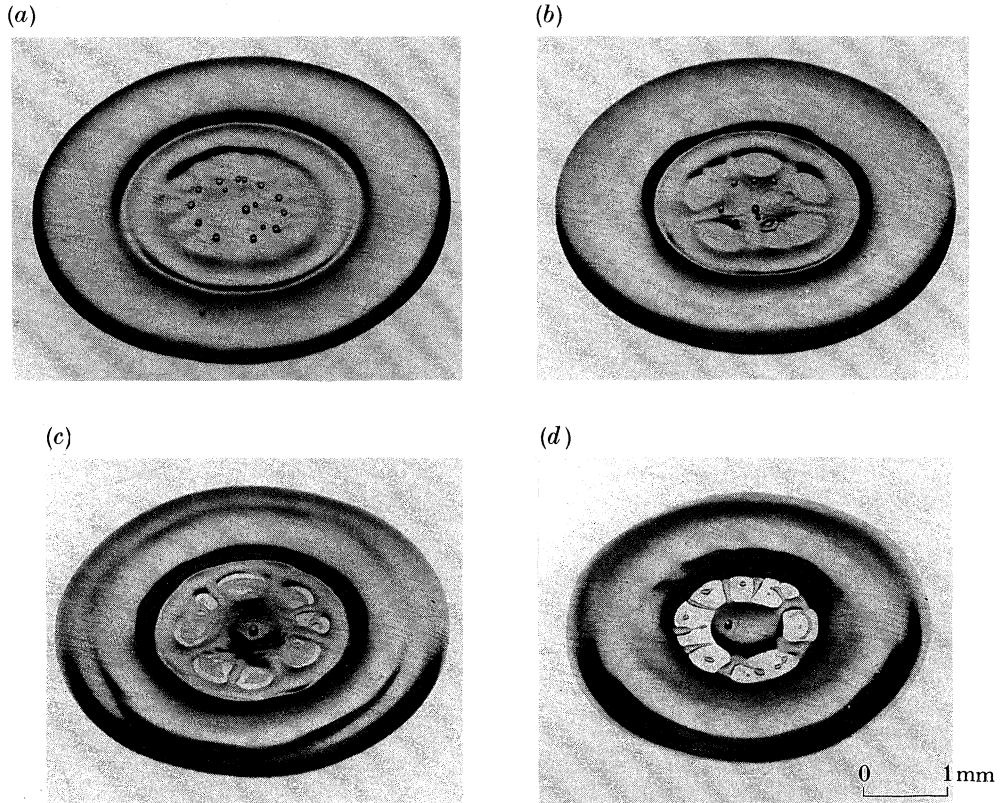


Figure 8. The impact of a n-heptane droplet on a stainless steel surface at 104 °C ($\alpha = 60^\circ$) showing (a) the formation of a bubble ring at $t = 5.6$ ms, (b) ridges on the liquid film at $t = 6.4$ ms, (c) cellular structures in the liquid film at $t = 7.2$ ms, and (d) evaporation of the liquid in the cellular structures at $t = 8.0$ ms.

described above can be seen more clearly, as well as the start of the formation of the ridges. At 6.4 ms ridges on the liquid surface begin to form. At 72 ms the ridges separating the dry patches formed a regular cellular pattern. The number of cells formed characteristically varied from six to ten. By 8.0 ms the liquid in the cells has evaporated while the ridges where the liquid film was thicker remain. The mechanism of vapour break-through to form dry patches could be that described by Burelbach *et al.* (1988). At 8.8 ms all the liquid in the ridges has evaporated, leaving behind a central bulb of liquid surrounded by an outer ring. Once the cells dry out there is no liquid pressure to restrain the inward motion of the liquid in the outer ring. Rewetting then occurred as shown in figure 7 with liquid flooding the region between the two rings. No further cell formation was seen after 8.8 ms. Enlargements showing the formation and subsequent evaporation of the cells are presented in figure 8*a-d*.

Figure 9 shows droplets impacting on a surface whose temperature is above the liquid boiling point ($T_s = 98.4$ °C). At $T_w = 100$ °C, no bubbles can be seen within the droplet at the solid-liquid interface. The surface superheat of 2 °C is insufficient to activate bubble nucleation in surface cavities. However, at $t = 0.8$ ms and $T_w = 180$ °C a cluster of bubbles apparently has formed in the drop. These bubbles correspond to the ring of bubbles seen in figure 6 at $t = 1.6$ ms for surface

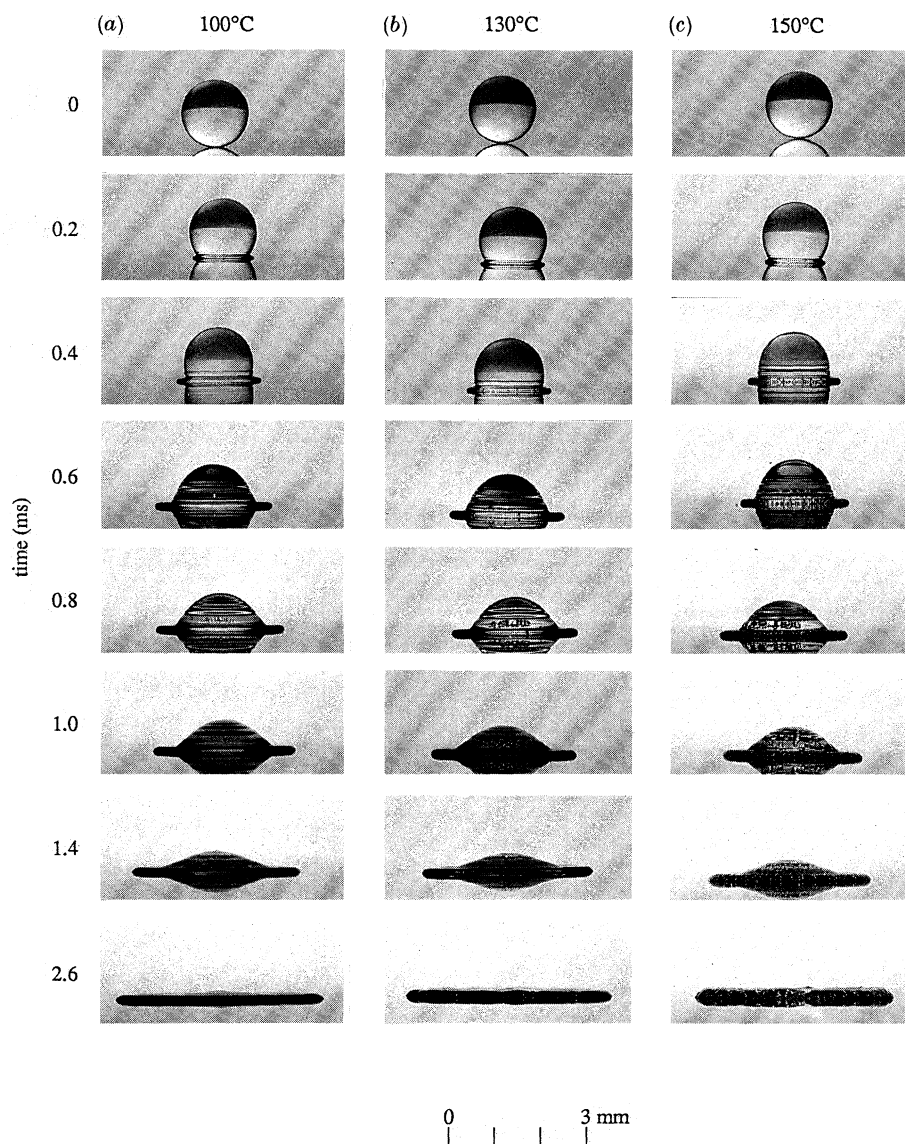


Figure 9. The impact on a n-heptane droplet on a heated stainless steel surface above the boiling point (98.4°C) of the liquid ($\alpha = 0^\circ$), (a) $T_w = 100^\circ\text{C}$, (b) $T_w = 130^\circ\text{C}$, and (c) $T_w = 150^\circ\text{C}$.

temperatures of 90°C and 104°C . These bubbles are probably caused by nucleation on impurities within the liquid rather than at nucleation sites on the heated surface because the bubbles appear to be in the bulk of the liquid instead of at the liquid–solid interface. For $T_w \geq 130^\circ\text{C}$ the surface temperature is hot enough for heterogeneous nucleation to occur at the surface, and bubbles can be seen at the solid–liquid interface in addition to those appearing in the bulk of the liquid (*cf.* $t = 0.8$ ms for $T_w = 130^\circ\text{C}$ and 150°C).

The transition from nucleate boiling to film boiling is shown in figure 10. The view is at $\alpha = 0^\circ$ in figure 1. At $T_w = 175^\circ\text{C}$ the pressure of the vapour below the liquid

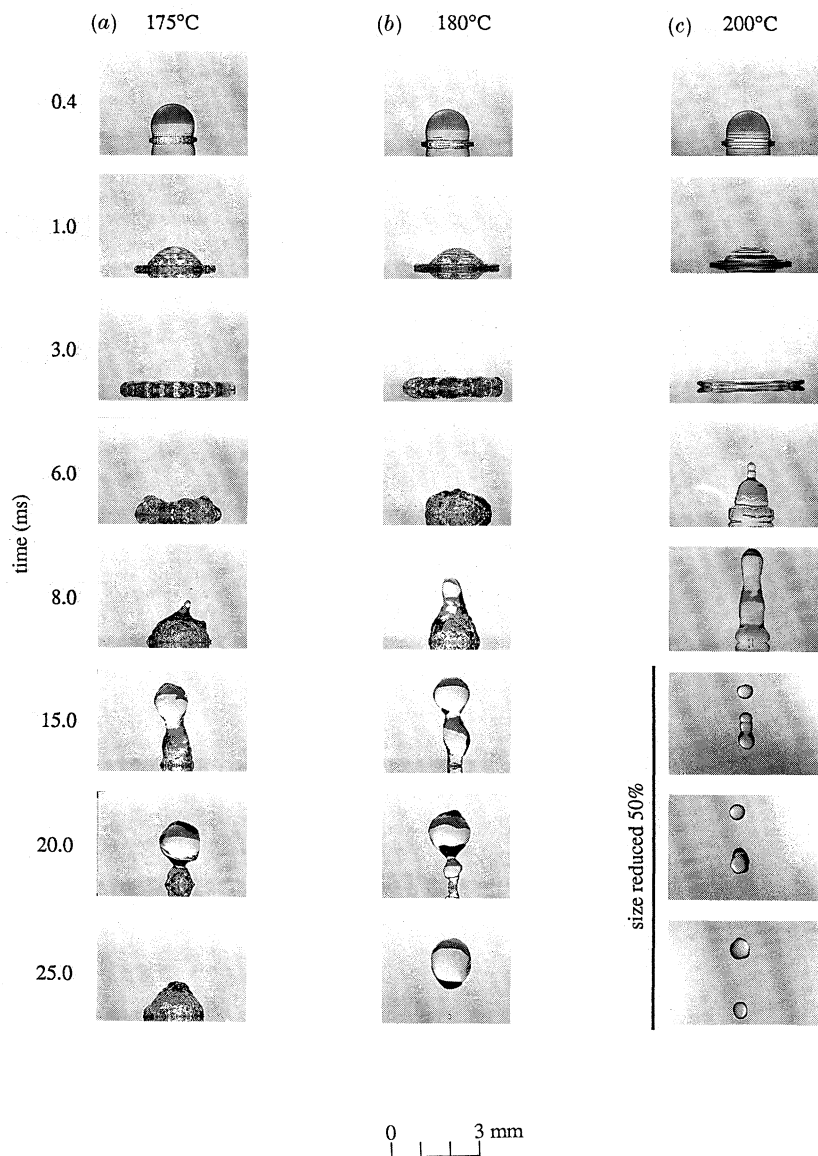


Figure 10. The transition from nucleate boiling to film boiling as T_w is raised above the Leidenfrost temperature (200 °C) of n-heptane ($\alpha = 0^\circ$) (a) $T_w = 175^\circ\text{C}$, (b) $T_w = 180^\circ\text{C}$, and (c) $T_w = 200^\circ\text{C}$.

was seen to partly lift the drop off the surface (e.g. $t = 15$ ms) and the droplet recoils on impact. This was the highest surface temperature at which there was always sustained liquid–solid contact, and it therefore corresponded to the minimum droplet evaporation time (*cf.* figure 5). A surface temperature of 180 °C was the minimum required to ensure that the pressure of the vapour was enough to at least partly levitate the droplet. Even though the droplet lifts off the surface at $T_w = 180^\circ\text{C}$ (figure 10*b* at $t = 25$ ms) there is still apparently intermittent solid–liquid contact as evidenced by the presence of bubbles inside the droplet. Additional photographs of the transition to film boiling are shown in figure 11 taken at $\alpha = 30^\circ$ to more clearly

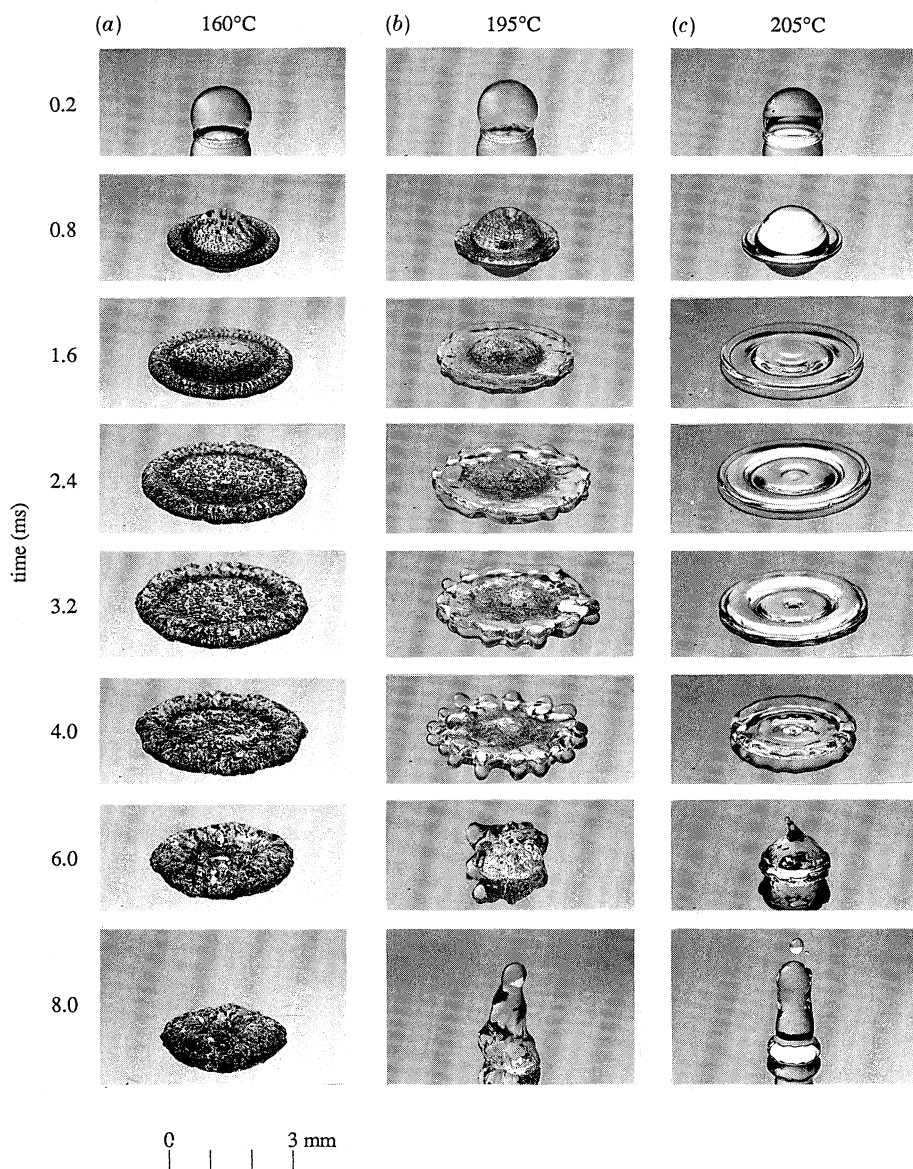


Figure 11. Additional views of the transition from nucleate boiling to film boiling ($\alpha = 30^\circ$)
 (a) $T_w = 160^\circ\text{C}$, (b) $T_w = 195^\circ\text{C}$, and (c) $T_w = 205^\circ\text{C}$.

show the extent of internal bubbling within the droplet. At $T_w = 160^\circ\text{C}$ large bubbles can be seen inside the droplet. $T_w = 195^\circ\text{C}$ corresponds to the upper limit of the transition boiling régime (figure 5).

The series of photographs shown in figure 11 provides some evidence that the appearance of bubbles within the droplet during impact when the surface is above the heptane boiling point is caused by heterogeneous nucleation on imperfections at the heated surface. Below the Leidenfrost temperature but above the heptane boiling point, numerous bubbles are inside the droplet (figures 9*b*, *c*, 10*a*, *b*, 11*a* and *b*). However, at $T_w = 205^\circ\text{C}$ (figure 11*c*) no bubbles are present because there is no

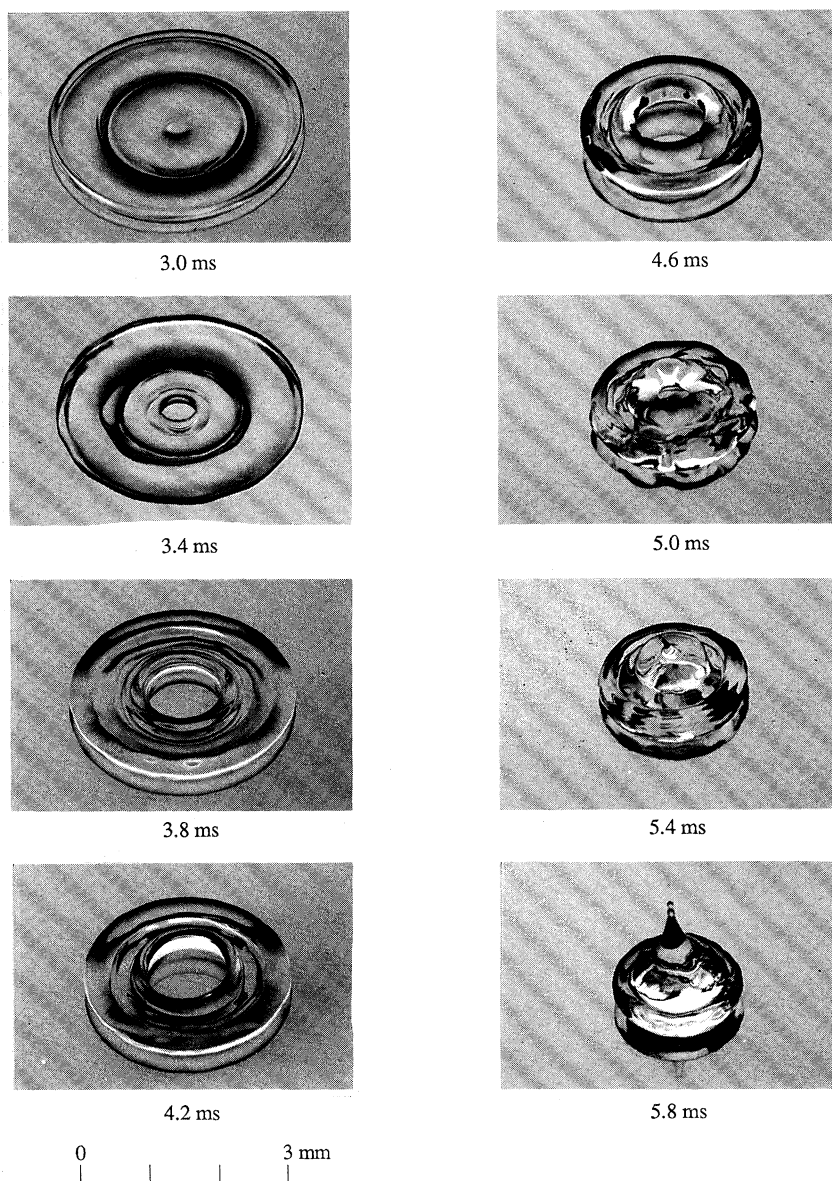


Figure 12. The formation of a hole in the centre of the liquid film during the spreading of a drop on a surface at 205 °C ($\alpha = 60^\circ$).

longer solid–liquid contact and therefore no opportunity for heterogenous nucleation to occur at the heated surface. The numerous bubbles that appear inside the droplet at higher temperatures are, therefore, probably caused by heterogeneous nucleation at the heated surface.

Above the Leidenfrost temperature the droplet experiences an evolution of its shape during impact which is similar to what occurs at lower temperatures, particularly in the early stages of impact. Compare, for example, the droplet shape 0.8 ms after impact in figures 6 and 11. This similarity of shape suggests a minimal

effect of liquid–solid contact and the attendant boundary conditions at the surface, and a predominance of the initial impact energy in the early stages, on the impact dynamics. This point is discussed further in §3.2.4.

The outwardly spreading liquid at $T_w > T_{\text{Leid}}$ creates a hole in the centre of the disc-shaped liquid as shown in figure 11*c*. Details of the formation of this hole are shown in figure 12 (photographed with $\alpha = 60^\circ$ to provide a better view of it.) At $t = 3$ ms the droplet has spread to its maximum extent. In subsequent photographs the outer diameter decreases as the droplet periphery retracts. However, the momentum of the liquid at the droplet centre keeps the liquid in the central region flowing outwards which increases the diameter of the hole. The opposing directions of motion of the inner and outer boundaries makes the liquid between them rise up in the form of ridges ($t = 4.2$ ms) and eventually creates a vertical jet (5.8 ms).

3.2. Comparison with theory

Analyses to predict various aspects of droplet impact have been previously published. These include predictions for the Leidenfrost temperature, the liquid superheat required for bubbles to form in the droplet, and the evolution of droplet shape. This section compares some of these analyses with the present experimental results.

3.2.1. Leidenfrost temperature

Spiegler *et al.* (1963) have identified the wall temperature at which film boiling begins – the Leidenfrost temperature – with the thermodynamic limit of superheat. This temperature is the maximum temperature that a liquid can sustain at a given pressure below the thermodynamic critical point without undergoing a phase transition (Avedisian 1985). The thermodynamic limit of superheat of a single component substance is defined by $\partial P/\partial V|_T = 0$, which for the van der Waals equation of state is

$$T_{\text{Leid}} = \frac{27}{32}T_C. \quad (1)$$

Baumeister & Simon (1973) added an empirical correction to (1) which accounts for the effect of surface cooling caused by the impact of the droplet:

$$T_{\text{Leid}} = \left[\frac{27}{32}T_C - T_L\right]/[\exp(0.00175\kappa)\text{erfc}(0.042\sqrt{\kappa})] + T_L, \quad (2)$$

where $\kappa = 1/(k\rho c)_{\text{surface}}$ ($\text{s cm}^4 \text{ }^\circ\text{C}^2 \text{ cal}^{-2}$). (3)

For n-heptane on a stainless steel surface (2) predicts $T_{\text{Leid}} = 205$ °C. This value is remarkably close to the measured value of 200 °C (figure 5), which in turn is also in reasonable agreement with the values of 190 °C reported by Fatehi (1986) and 182 °C reported by Tamura & Tanasawa (1959).

3.2.2. Liquid superheat

The origin of bubbles within the droplets is believed to be nucleate boiling on the surface when the surface temperature is above the heptane saturation temperature. The bubbles emerge from the mouth of surface imperfections, break free from the surface, and then migrate through the bulk of the droplet.

A model to predict the incipient superheat for bubble formation within a droplet impacting a surface was presented by Iloeje *et al.* (1975) in the limit of a ‘soft’ deposition (i.e. $We \rightarrow 0$). Figure 13 shows the thermal model. The liquid and solid are assumed to be semi-infinite and to be brought into contact with each other at time

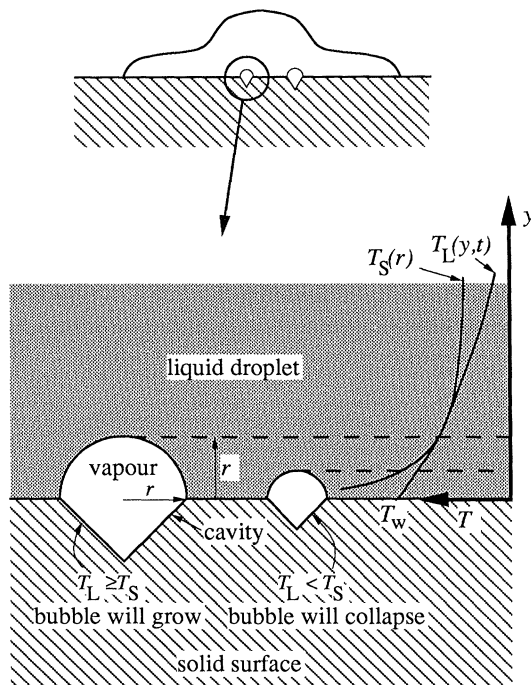


Figure 13. Model for bubble nucleation in a surface cavity.

$t = 0$. The model further assumes that the radius of an incipient bubble is the same as the cavity opening which characterizes the surface imperfections. The liquid pressure is assumed to be constant (which, therefore, precludes a bubble from forming by cavitation by this model). Bubbles that continue to grow when they reach the mouth of the cavity will detach and rise up in the droplet. For this to happen the temperature of the liquid at the bubble surface at a distance r from the surface (*cf.* figure 13) must be greater than that of the gas inside the bubble (which is approximately the saturation temperature, T_s).

To illustrate the capabilities of this model in the context of the present experimental results, we assume that the maximum cavity diameter on the stainless steel surface, which defines the minimum superheat, is $1.5 \mu\text{m}$ (based on the typical surface roughness of a ground steel surface). For this dimension, surface nucleation sites are predicted to be activated (*i.e.* bubbles will form) when $T_w \geq 104^\circ\text{C}$ for a droplet of *n*-heptane. As a result, no bubbles would be expected to form at the liquid–solid interface for $T_w = 100^\circ\text{C}$ even though the heptane saturation temperature is 98°C . Bubbles should be seen at higher temperatures, which is in agreement with the present observations (*cf.* figures 9 and 11*a*).

3.2.3. Droplet shape

Analyses to predict the evolution of the shape of droplets impacting on solid surfaces have been presented by Savic & Boulton (1955), Harlow & Shannon (1967), and Huang *et al.* (1973). The continuity and momentum equations were solved either analytically or numerically. Surface tension and viscosity were neglected.

Neglecting liquid compressibility, the predicted droplet shapes were shown to have a universal form independent of liquid properties. The droplet shape is only a

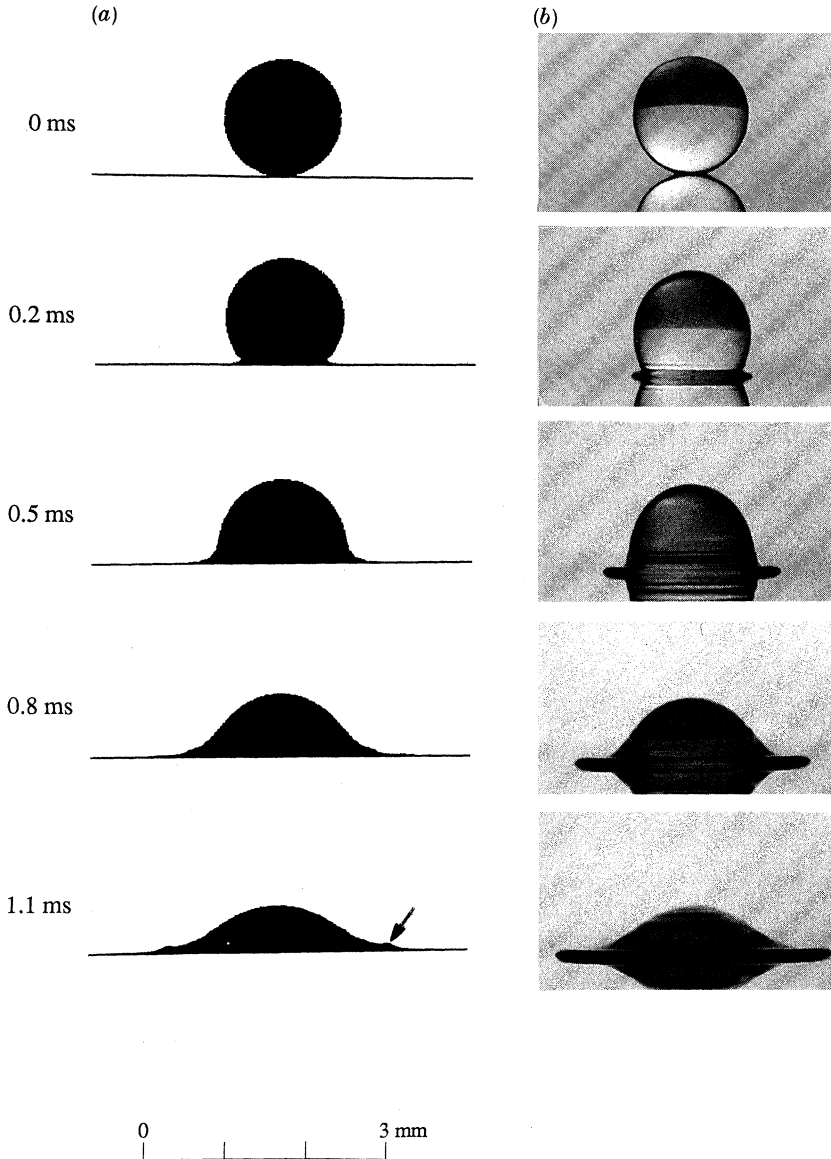
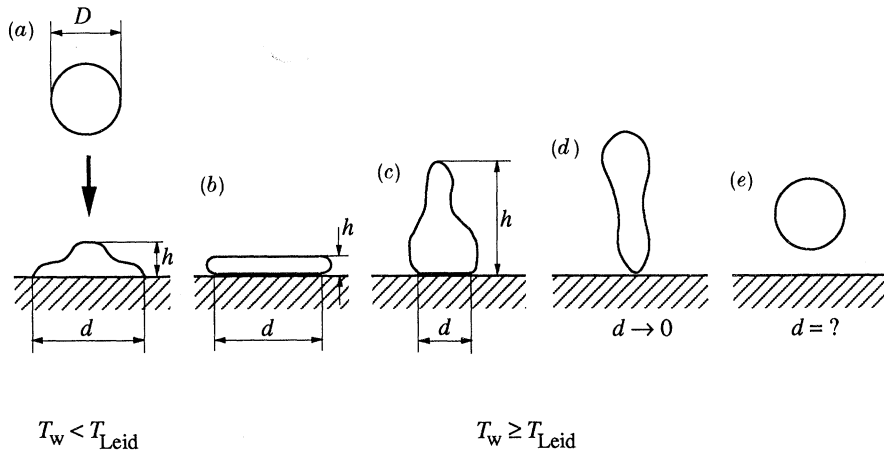


Figure 14. Comparison of (a) the results from the model of Harlow & Shannon (1967) with (b) experimental observations from the present study of the evolution of droplet shape during the impact of a droplet on a surface at 24 °C.

function of a dimensionless time, (Ut/D) . Harlow & Shannon (1967) calculated these universal shapes (the calculated shapes are cross sectional images) and figure 14 compares them with some of the present experimental observations. The photographs shown in figure 14 were taken at $\alpha = 0^\circ$ to provide a clearer view of the film structure.

As shown in figure 14, the analysis predicts the basic features of the jet observed in the experiment for the early times shown in figure 14. However, several facts to note are the following: (1) the film is predicted to spread without bound in the analysis whereas in reality the film eventually stops moving (or retracts) because the

Figure 15. Definition of d and h .

internal pressure which drives the motion, initially, dissipates as spreading proceeds until the pressure cannot overcome the resistance to this motion due to viscous effects at the solid–liquid interface, (2) the analysis predicts the existence of a wave in the advancing jet which seems to be moving within the film (*cf.* the ridge marked by an arrow in figure 14*a* at $t = 1.1$ ms), and (3) the existence of the jet is predicted through the jet structure is different than observed.

3.2.4. Spreading rate

Two dimensions are used to characterize droplet spreading: the diameter of the wetted area, and the droplet height above the surface h (figure 15). Normalizing these quantities by the initial droplet diameter (D) yields the so-called ‘spread factor’ $\beta(t) \equiv d(t)/D$ (Bonacina *et al.* 1979; diMarzo & Evans 1989) and the dimensionless height $\zeta(t) \equiv h(t)/D$.

The definition of β is unambiguous when $T_w < T_{Leid}$. When $T_w > T_{Leid}$, the droplet no longer wets the surface. $d(t)$ was then defined as the diameter of the flattened area covered by the drop at the solid–liquid interface (figure 15*b*) during deformation for this case. If the droplet recoils from the surface (figure 15*c* and *d*) when $T_w > T_{Leid}$, d can approach zero (figure 15*c*). And, for a spherical droplet in steady Leidenfrost evaporation, d would be undefined (figure 15*d*) by this definition. Our measurements of the diameter of the wetted area, therefore, were restricted only to the period of impact and first recoil at $T_w > T_{Leid}$.

Figure 16 shows the evolution of measured values of β . Figure 16*a* displays measurements with the surface temperature as the parameter. The data in figure 16*b* provide an expanded view of the early time domain (0 to 2.5 ms) at a surface temperature of 24 °C. Also shown in figure 16*b* are data for spreading on a pre-existing liquid film created by deposition of a single 1.5 mm diameter droplet. It is interesting that β and ζ for a droplet spreading on a thin liquid film is essentially the same as on a solid surface during this early period. This result can be attributed to the negligible influence of surface tension and viscous effects at the surface during the early stage of impact, as discussed below.

The spread factor and spreading rate, $d\beta/dt$, are independent of surface temperature in the early period of impact, $t < 2$ ms, and are in agreement with the

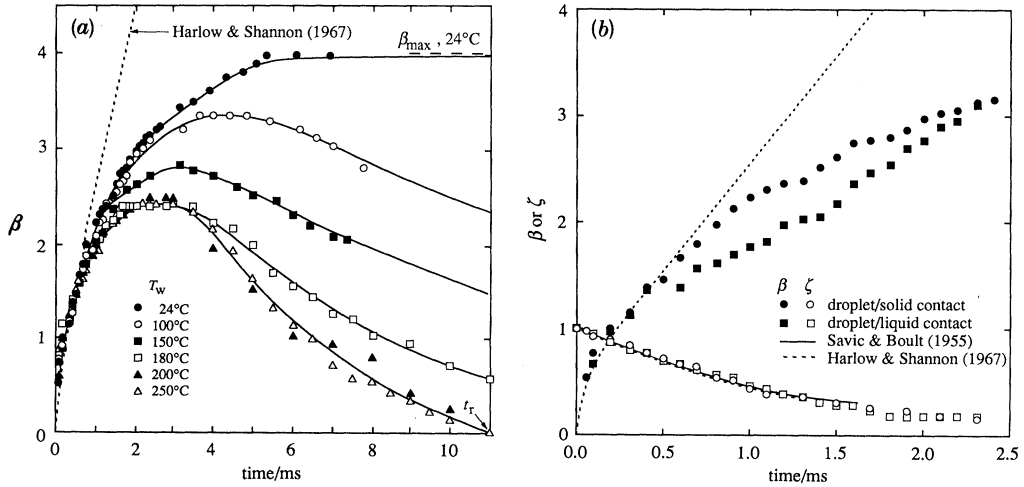


Figure 16. (a) Evolution of β during the impact of a droplet on a hot surface for several values of T_w . (b) Comparison of theoretical predictions with experimental observations for the evolution of β and ζ .

predictions of Harlow & Shannon (1967) and Savic & Boulton (1955) in which viscous and surface tension effects were assumed to be negligible. To show that viscous and surface tension forces are indeed negligible during the early stages of impact under the present experimental conditions, the relative magnitude of the forces acting on the droplet during impact and spreading is estimated.

The forces per unit area restraining the radial outflow of liquid from the point of impact are due to viscous shear at the liquid–solid interface (Huh & Scriven 1971),

$$\tau = \mu \partial v_x / \partial y \approx \mu U / h \quad (4)$$

(the sideways jetting velocity is assumed to be of the same order of magnitude as the impact velocity U), and the interfacial tension pressure,

$$P_\sigma \approx 2\sigma / r_i. \quad (5)$$

The effect of the contact angle is incorporated in r_i in (5).

The order of magnitude of stagnation pressure in the droplet after impact, which drives the radial flow of liquid, is

$$P_s \approx \frac{1}{2} \rho U^2. \quad (6)$$

Assuming that the stagnation pressure acts on an area of length proportional to h , and that the shear stress acts on an area of length proportional to d , the ratio of the stagnation pressure force to the viscous force (Ψ) can be obtained by combining equations (4) and (6) to give

$$\Psi \approx \frac{2}{3} Re / \beta^5 \quad (7)$$

where use has been made of the equivalence of volume between the spherical droplet and the liquid after it has flattened into the shape of a disc (neglecting the contribution to the disc volume due to the curvature of the edges).

The ratio of the stagnation pressure force to the surface tension force (Δ) is obtained by combining equations (5) and (6):

$$\Delta \approx \frac{1}{6} We / \beta^2. \quad (8)$$

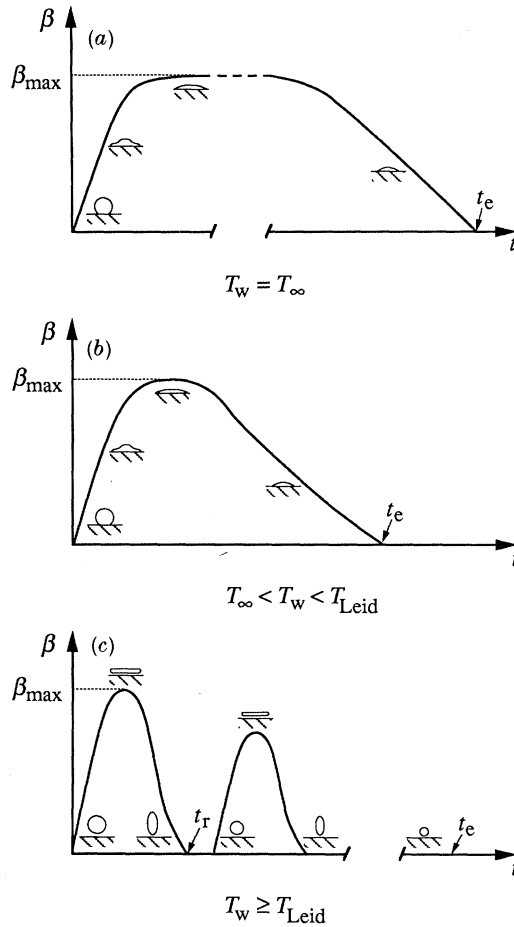


Figure 17. Variation in the evolution of β with surface temperature for (a) $T_w = T_\infty$, (b) $T_\infty < T_w < T_{Leid}$, and (c) $T_w \geq T_{Leid}$.

In (8) the radius of curvature of the liquid–solid interface (r_i), has been assumed to be proportional to h . This assumption will give the maximum value of P_σ late in the impact, since $r_i \geq h$ when the drop is flattened in the shape of a disc.

If $\Psi \gg 1$ and $\Delta \gg 1$, both viscous and surface tension forces per unit area are negligible compared with the stagnation pressure force. In the present experiments, $We = 43$, $Re = 2300$, and $\beta < 1$ (figure 16b) in the early stages of impact. Therefore $\Delta > 7$, $\Psi > 500$ and the model assumptions are approximately valid. The present data are therefore well predicted (figure 16). As time advances, β increases and can reach an extremum under certain conditions depending on the surface temperature (figure 16a) due to dynamic recoil and/or evaporation of the advancing jet. Taking at later times $\beta \approx 0.4$, we have that $\Delta \approx 4$ and $\Psi \approx 0.5$. Larger deviations between measured and predicted values of β and ζ are therefore expected. Such deviations are shown in figure 16.

The evolution of β varied in three different ways, depending on the surface temperature. Firstly, if the surface is at the ambient temperature ($T_w = T_\infty$), then β increases monotonically until it reaches a maximum (figure 17a) after which it may

decrease because of the drop recoiling (if We is large) or evaporation at the contact line. Secondly, if $T_\infty < T_w < T_{Leid}$ (figure 17*b*) β first increases as the droplet spreads out and then decreases as the liquid begins to evaporate and/or recoil. This behaviour is illustrated in figure 16*a* by the data corresponding to $T_w = 100^\circ\text{C}$ and 150°C . β exhibits a peak approximately 4 ms after impact at this temperature. The extremum in β can also be seen in the photographs of figure 6 for $T_w = 90^\circ\text{C}$ and 104°C ; the film diameter appears to be the largest at $t = 3.2$ ms. Thirdly, for $T_w \geq T_{Leid}$ (figure 17*c*) the evolution of β can exhibit multiple peaks (the first only of such peaks is illustrated by the data displayed in figure 16*a*) because of recoil/rebound/evaporation of the drop from the surface (figure 10*c*). Repeated rebound and impact can give rise to the 'scallop'-like behaviour that is schematically illustrated in figure 17*c*.

When $T_w \geq T_{Leid}$, the time period of recoil/impact has been suggested to be of the order of the vibration period of a freely oscillating droplet (Wachters & Westerling 1966):

$$t_r = \pi[\rho d^3/(16\sigma)]^{\frac{1}{2}}. \quad (9)$$

In (9) t_r depends on temperature through the variation of surface tension and density of the droplet with temperature. The droplet temperature will be approximately constant for the range of solid surface temperatures studied, and in any case will not exceed the wet bulb temperature of the liquid. Thus, the primary parameter in (9) is the droplet diameter, and for constant d as in the present experiments, t_r is constant. To illustrate, figure 16*a* shows that at wall temperatures of 200°C and 250°C (which are close to and above T_{Leid} , respectively) the rebound time has a unique value (about 11 ms in this case) as expected because the initial diameter was uniform for the data displayed in figure 16. The predicted rebound time from (9) is 8.3 ms.

An expression for the maximum value of β can be obtained from a simple energy balance for the case of no bubbles inside the droplet. The presence of bubbles complicates the definition of the contact angle at the edge of the advancing liquid front (see insets to figure 18) as discussed below. The droplet shape at β_{max} is modelled as a disc because this shape is close to the observed shape as shown by the planar views in figures 2 and 10. The contribution to the total surface area of the liquid by the curved edge of the boundary of the liquid film is neglected. It is also assumed that the droplet volume is constant so that the results are not applicable if there is significant evaporation of liquid during the period over which β increases to β_{max} .

Before impact, the kinetic energy (E_{K1}) and surface energy (E_{S1}) of the spherical drop are given by

$$E_{K1} = (\frac{1}{2}\rho U^2) (\frac{1}{6}\pi D^3), \quad (10)$$

$$E_{S1} = \pi D^2 \sigma. \quad (11)$$

After impact, the kinetic energy is expended by deforming the droplet, and it is zero at the maximum extension diameter. The surface energy (E_{S2}) at d_{max} is (Ford & Furmidge 1967)

$$E_{S2} = (\frac{1}{4}\pi d_{max}^2) \sigma(1 - \cos \theta). \quad (12)$$

The contact angle is here taken to be defined by the intersection of the tangent line at the liquid-vapour interface, at the point where the meniscus begins, with the wall (figure 18).

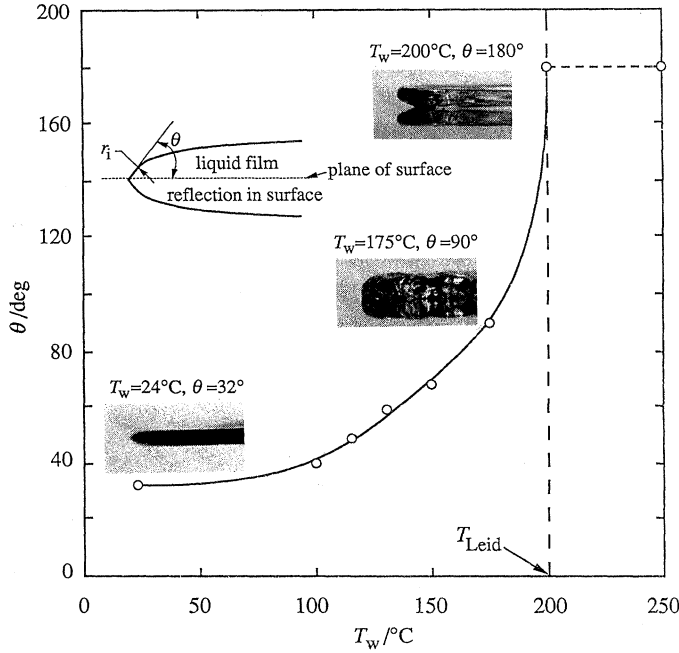


Figure 18. Variation of θ with T_w . The insets show photographs of the tip of the spreading liquid film, from which measurements of θ were made.

The energy (W) lost in deforming the drop against viscosity is, approximately,

$$W = \int_0^{t_c} \int_V \phi \, dV \, dt \approx \phi V t_c. \quad (13)$$

The dissipation function ϕ is given by

$$\phi = \mu \left(\frac{\partial v_i}{\partial x_j} + \frac{\partial v_j}{\partial x_i} \right) \frac{\partial v_i}{\partial x_j} \approx \mu \left(\frac{U}{h} \right)^2. \quad (14)$$

t_c is estimated by assuming it to be the time taken for the droplet height h to go from its maximum value of D to 0 at velocity U . Hence

$$t_c \approx D/U. \quad (15)$$

The volume of the liquid in the drop, once it has flattened out in the shape of a disc, is

$$V \approx \frac{1}{4} \pi d_{\max}^2 h. \quad (16)$$

Combining (13)–(17) yields

$$W \approx \frac{1}{4} \pi \mu (U/h) D d_{\max}^2. \quad (17)$$

From energy conservation, $E_{K1} + E_{S1} = E_{S2} + W$. Hence,

$$\frac{3}{2} \frac{We}{Re} \beta_{\max}^4 + (1 - \cos \theta) \beta_{\max}^2 - \left(\frac{1}{3} We + 4 \right) \approx 0. \quad (18)$$

When $Re \rightarrow \infty$, $\beta_{\max} \approx [(\frac{1}{3} We + 4)/(1 - \cos \theta)]^{\frac{1}{2}}$. Above T_{Leid} the apparent contact angle is considered to be fixed at 180° (Fiedler & Naber 1989), from which it is seen that

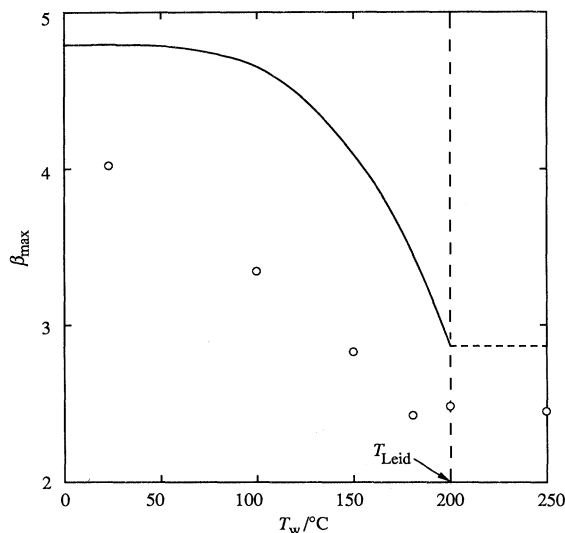


Figure 19. Comparison of predicted (line) with observed (circles) variation of β_{\max} with T_w .

(18) reduces to $\beta_{\max} = (\frac{1}{3}We + 4)^{\frac{1}{2}}$ when again the Reynolds number is large. Several correlations for β_{\max} of this form have been reported (Ueda *et al.* 1979; Akao *et al.* 1980). In the present experiments viscous losses are low compared with surface tension forces as shown by the fact that W is approximately 4% of E_{s2} . However, if the droplet is small or the liquid viscosity high, Re may be small and viscous losses could then be significant.

Measurements of β_{\max} (figure 16a) show that it decreases with increasing wall temperature. For (18) to yield this trend, θ must increase with increasing T_w because the variation of β_{\max} with T_w is carried primarily in the dependence of θ with T_w in (18). An analysis by Wayner (1989) can be used to illustrate the effect of T_w on θ .

Using a simple conduction model for heat transfer across the extended meniscus and assuming that all of the liquid flowing into the meniscus at the rate Γ evaporates, we have that

$$k(T_w - T_b)/\delta = \Gamma h_{fg}, \quad (19)$$

where δ is the film thickness. The mass flow rate of liquid into the meniscus in the region where disjoining pressure predominates can be written as (Wayner 1989)

$$\Gamma \approx |A| (d\delta/dx)/(\nu\delta), \quad (20)$$

where A is the Hamaker constant. Noting that $\tan(\theta) \approx d\delta/dx$, (19) and (20) combine to yield

$$\theta \approx \arctan [k(T_w - T_b)\nu/(h_{fg}|A|)] \quad (21)$$

from which it is seen that the apparent contact angle increases with increasing T_w .

The contact angle was measured from enlarged views of the advancing liquid film. Figure 18 shows the results, as well as the shape of the advancing liquid film at three different surface temperatures. The results show that θ does in fact increase with increasing wall temperature. Near T_{Leid} it is noted that the measurement and definition of θ is complicated by bubbles within the film and the disturbances they create in the contact line. The bubbles will increase the thickness of the film by expanding its volume rather like foaming (*cf.* the insets to figure 18), and, thus, the apparent value of the contact angle.

A polynomial curve of best fit was passed through the data in figure 18 (*cf.* the curve in figure 18) and (18) was then used to obtain predictions of β_{\max} with this fit. $Re = 2300$ and $We = 43$ were used in (18) because these values characterized our experiment. Figure 19 compares the predicted variation of β_{\max} with wall temperature with measured values (obtained from figure 16*a*). Reasons for discrepancies may be that the energy dissipated during droplet deformation is underestimated by (17), or that a significant amount of liquid may be lost through evaporation during impact (which is neglected in the analysis).

Above the Leidenfrost temperature (18) shows that β_{\max} should be constant if the apparent contact angle is constant (Re and We being held constant). Figures 16*a* and 19 do illustrate the convergence of β_{\max} above T_{Leid} . The measured β_{\max} is about 2.4 while (18) yields $\beta_{\max} \approx 2.9$.

We thank Professor P. C. Wayner of the Rennselaer Polytechnic Institute for various discussions. This work was supported by the National Science Foundation (grant no. CBT-8451075), the Semiconductor Research Corporation, and the New York State Center for Hazardous Waste Management.

References

- Akao, F., Araki, K., Mori, S. & Moriyama, A. 1980 *Trans. Iron Steel Inst. Japan* **20**, 737–743.
- Avedisian, C. T. 1985 *J. Phys. Chem. Ref. Data* **14**, 695–720.
- Baumeister, K. J. & Simon, F. F. 1973 *J. Heat Transfer* **95**, 166–173.
- Block, M. J. 1956 *Nature, Lond.* **178**, 650–651.
- Bonacina, C. & Del Giudice, S. 1979 *J. Heat Transfer* **101**, 441–446.
- Brunton, J. H. & Camus, J. J. 1970 *Proc. 3rd Int. Conf. on Rain Erosion*, pp. 327–347.
- Burelbach, J. P., Bankoff, S. G. & Davis, S. H. 1988 *J. Fluid Mech.* **195**, 463–494.
- Chandra, S. 1990 Ph.D thesis, Cornell University.
- Cook, R., Tung, C. Y. & Wayner, P. C. 1981 *J. Heat Transfer* **103**, 325–330.
- diMarzo, M. & Evans, D. D. 1989 *J. Heat Transfer* **111**, 210–213.
- Edgerton, H. E. 1979 *Electronic flash strobe*, 2nd edn. Cambridge: The MIT Press.
- Engel, O. G. 1955 *J. Res. natn. Bur. Stand.* **54**, 281–298.
- Fatehi, M. 1986 M.S. thesis, Cornell University.
- Fiedler, R. & Naber, J. 1989 Spring Meeting, Central States Section, Combustion Institute, April 30 to May 2. Dearborn, Michigan.
- Ford, R. E. & Furmidge, C. G. L. 1967 *Wetting*, Soc. Chem. Industry Monograph no. 25, pp. 417–432.
- Harlow, F. H. & Shannon, J. P. 1967 *J. appl. Phys.* **38**, 3855–3866.
- Huang, Y. C. & Hammitt, F. G. 1972 *Proc. ASME Polyphase Flow Forum* **1**, 9–10.
- Huang, Y. C., Hammitt, F. G. & Yang, W. J. 1973 *J. Fluids Eng.* **95**, 276–294.
- Huh, C. & Scriven, L. E. 1971 *J. Colloid Interface Sci.* **35**, 85–101.
- Inada, S., Miyasaka, Y., Nishida, K. & Chandratilleke, G. R. 1983 *Proc. ASME-JSME Thermal Engineering Joint Conf.* vol. 1, 173–182.
- Iloeje, O. C., Rohsenow, W. M. & Griffith, P. 1975 *ASME Paper No. 75-WA/HT-1*.
- Longuet-Higgins, M. S. 1990 *J. Fluid Mech.* **214**, 395–410.
- Nishio, S. & Mirata, M. 1978 *Proc. 6th Int. Heat Transfer Conf.*, Toronto, **1**, 245–250.
- Savic, P. 1958 *Nat. Res. Council Canada*, Rep. no. MT-37.
- Savic, P. & Boulton, G. T. 1955 *Nat. Res. Council Canada*, Rep. no. MT-26.
- Spiegler, P., Hopenfeld, J., Silberberg, M., Bumpus, C. T. & Norman, A. 1963 *Int. J. Heat Mass Trans.* **6**, 987–989.
- Tamura, Z. & Tanasawa, Y. 1959 *7th Symposium (Int.) on Combustion*, pp. 509–522. London: Butterworths.

- Toda, S. 1974 *Heat Transfer Jap. Res.* **3** (1), 1–44.
- Wachters, L. H. J. & Westerling, N. A. J. 1966 *Chem. Eng. Sci.* **21**, 1047–1056.
- Wayner, P. C. 1989 *J. Heat Transfer* **111**, 813–815.
- Worthington, A. M. 1877*a* *Proc. R. Soc. Lond.* **25**, 261–271.
- Worthington, A. M. 1877*b* *Proc. R. Soc. Lond.* **25**, 498–503.
- Worthington, A. M. 1908 *A study of splashes*. London: Longmans, Green and Co.
- Yao, S. C. & Cai, K. Y. 1988 *Exp. Thermal Fluid Sci.* **1**, 363–371.
- Yiantsios, S. G. & Davis, R. H. 1989 *Bull. Am. phys. Soc.* **34**, 2323.

Received and accepted 23 July 1990

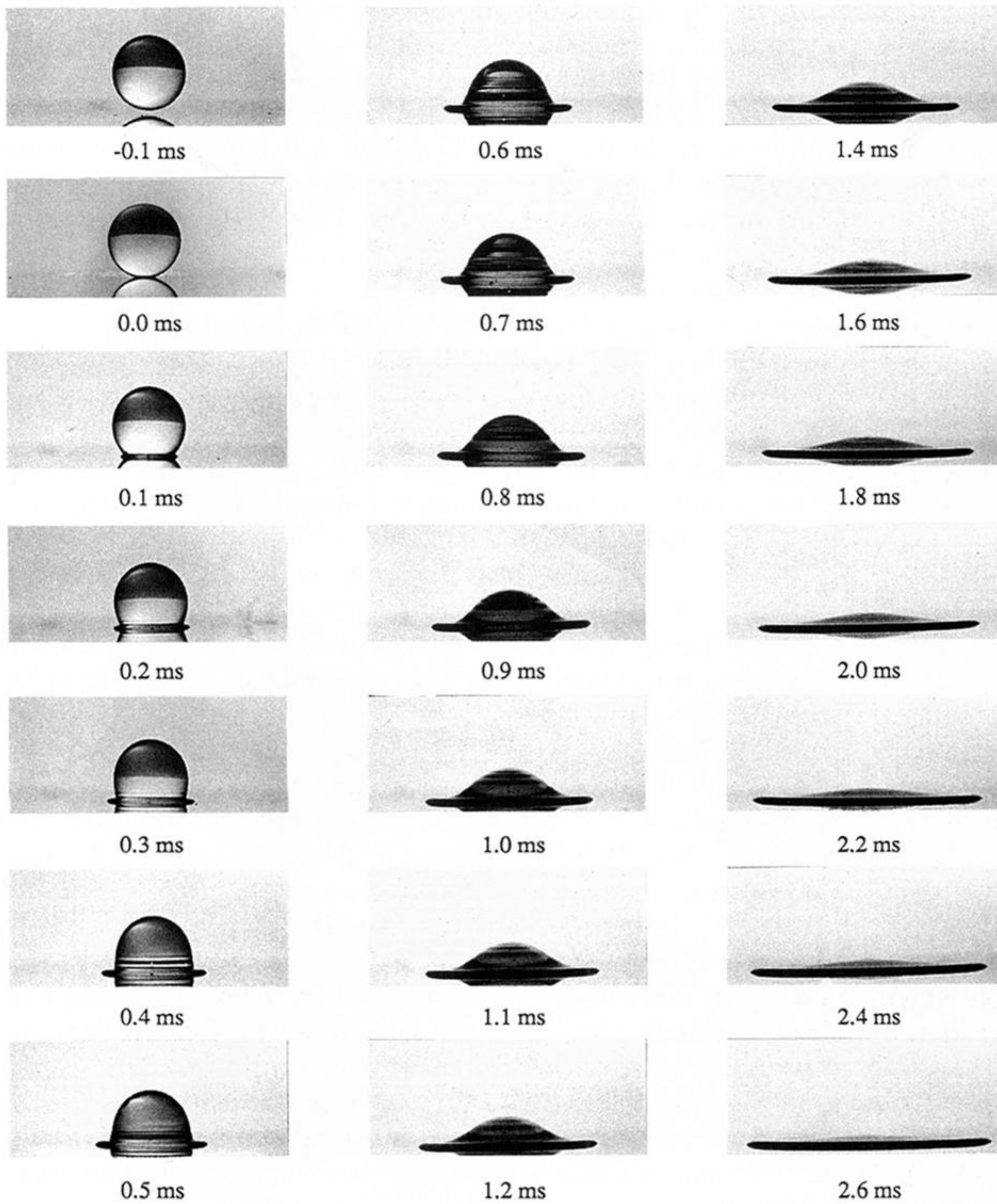
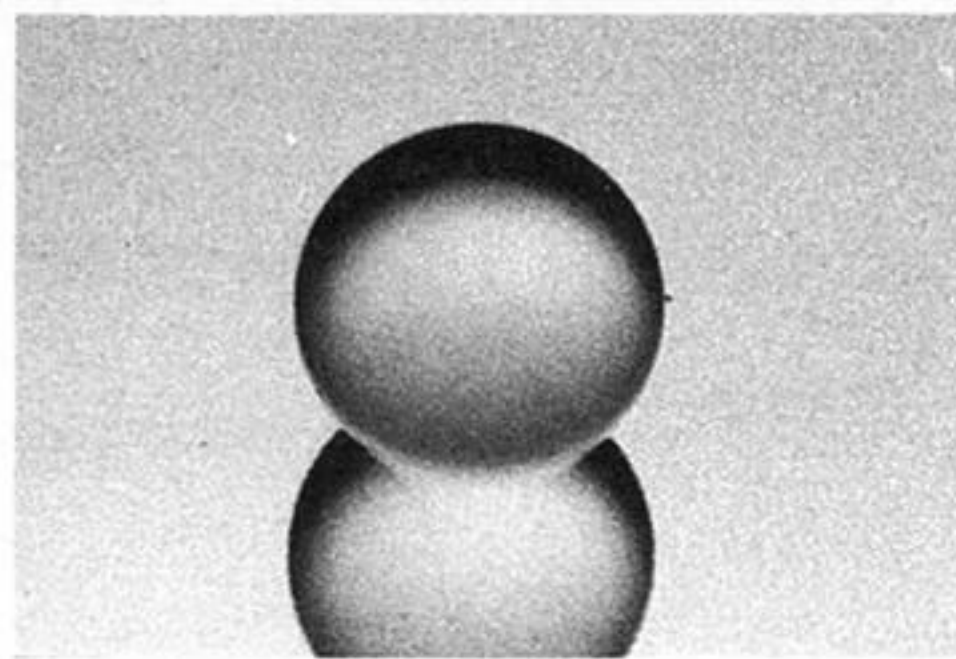
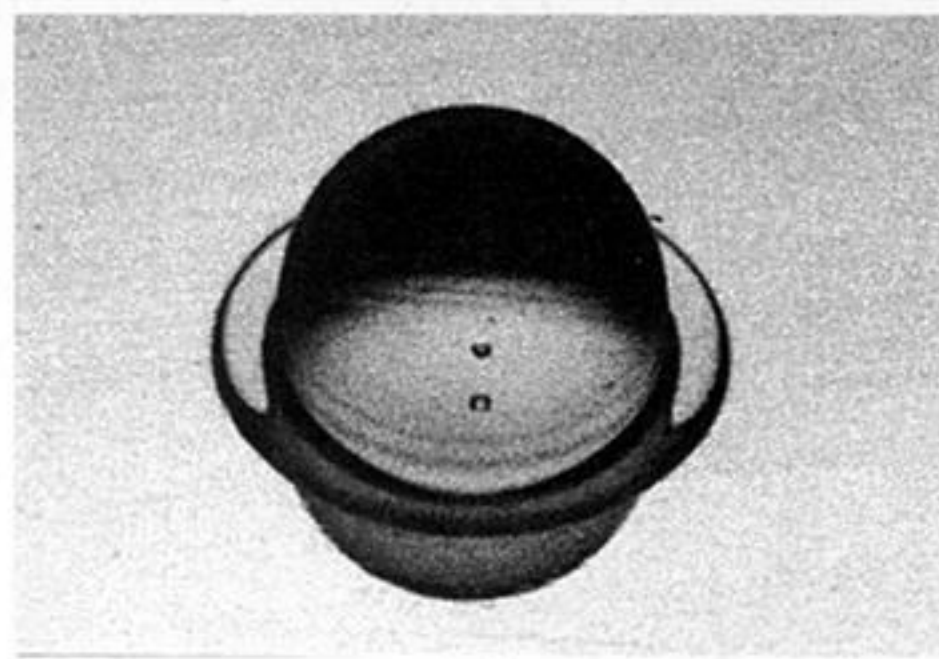


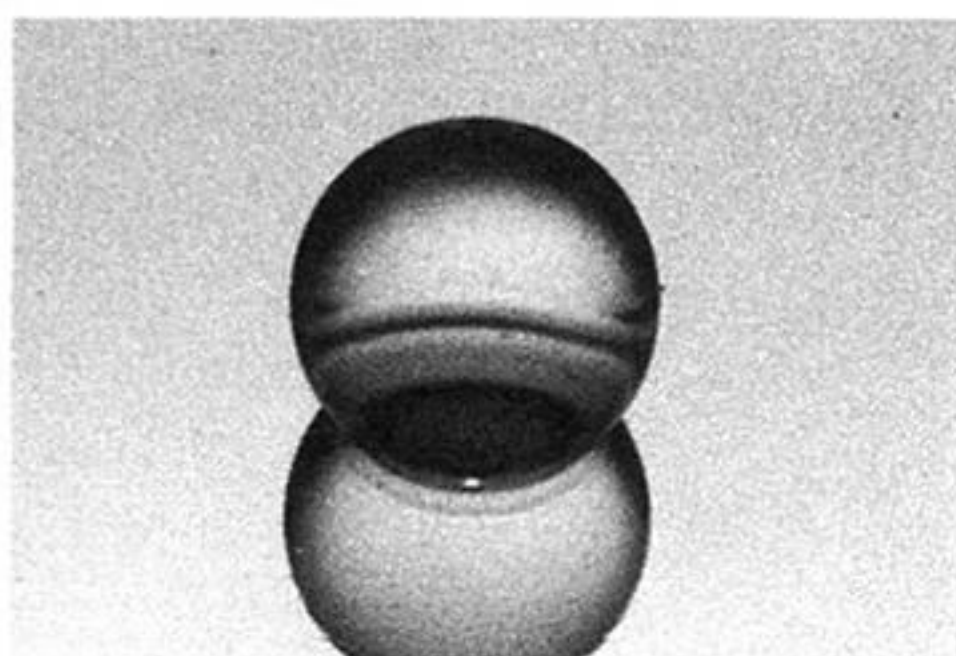
Figure 2. The impact of a n-heptane droplet on a stainless steel surface at 24 °C ($\alpha = 0^\circ$).



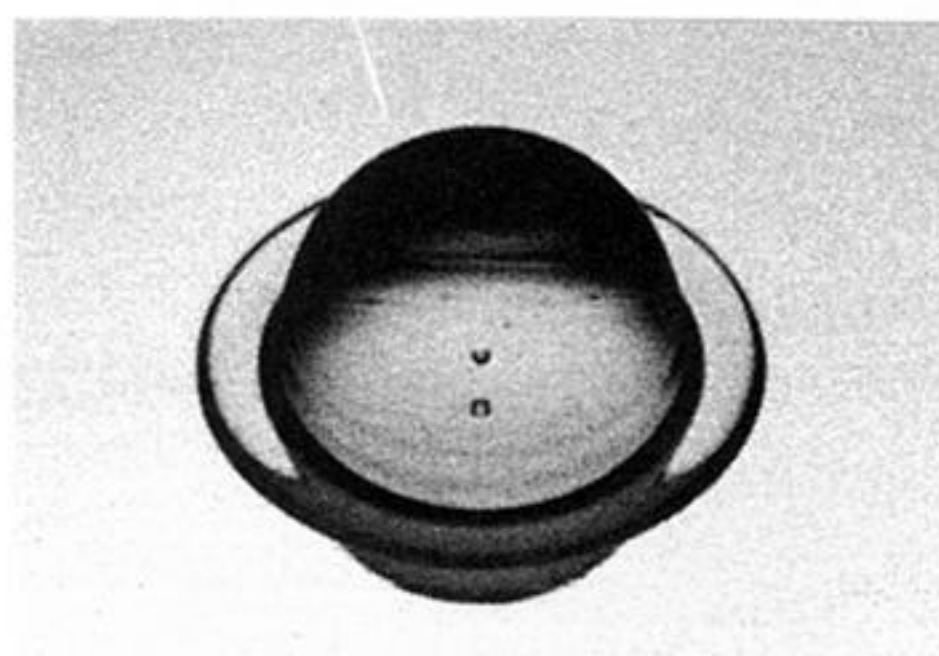
0 ms



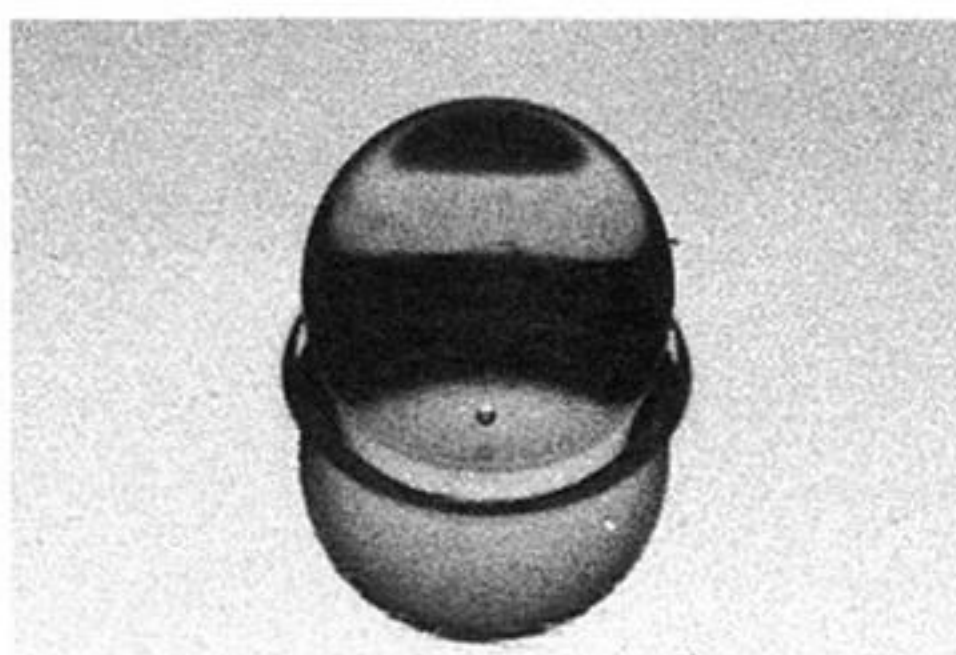
0.4 ms



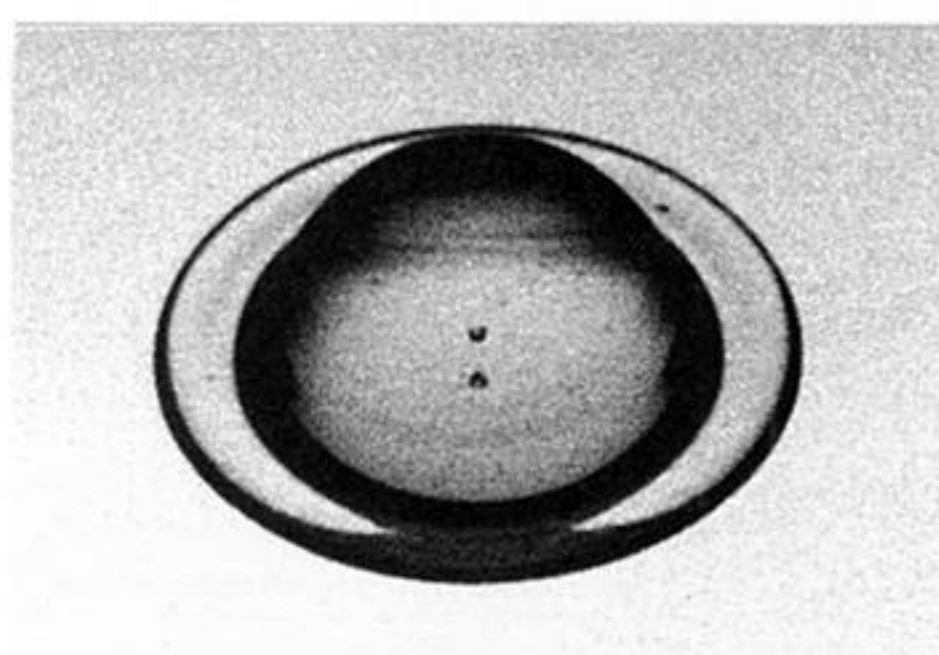
0.1 ms



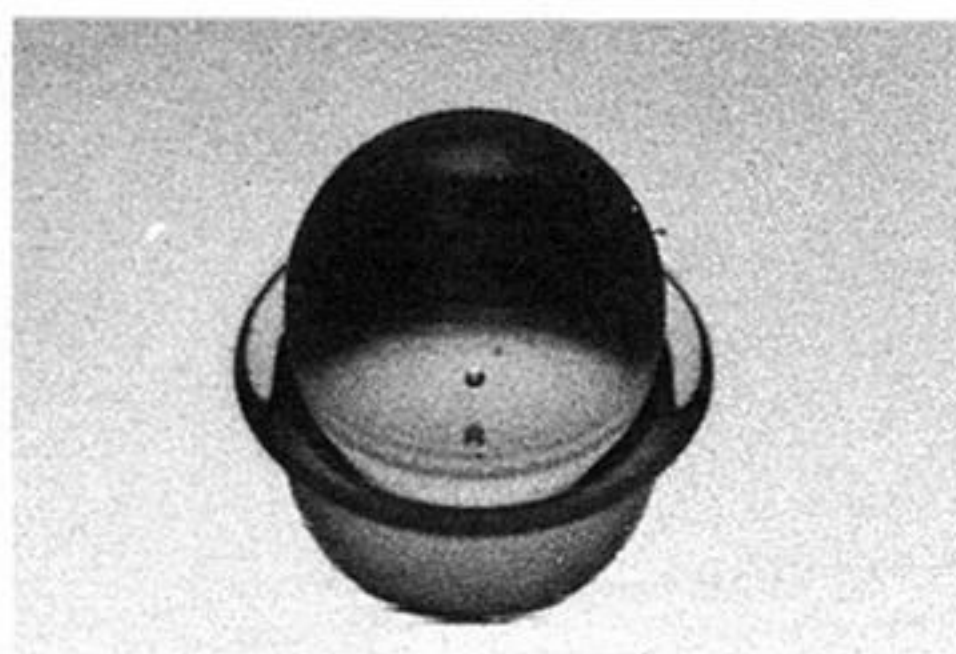
0.5 ms



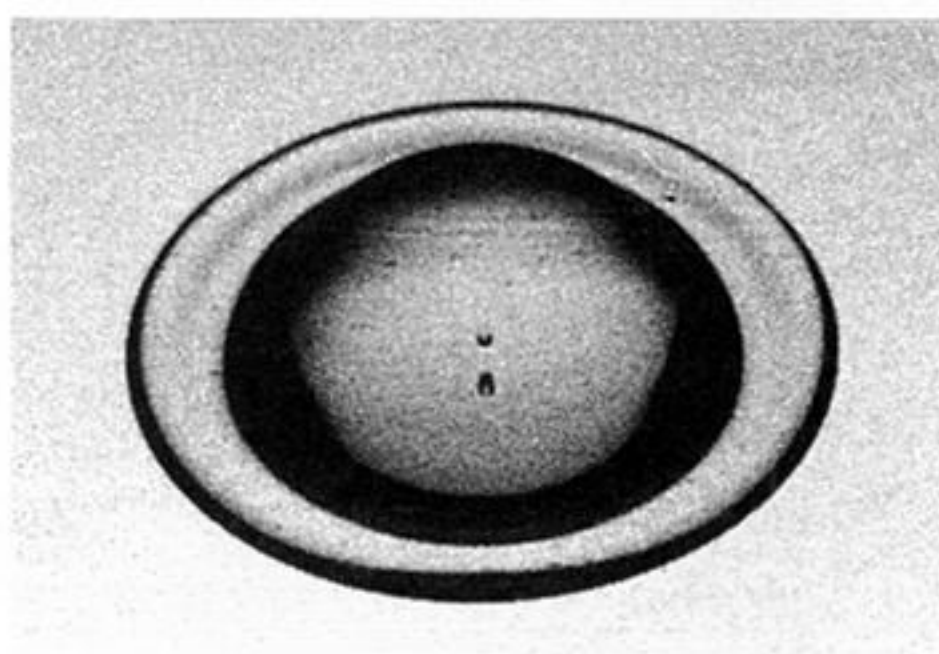
0.2 ms



0.6 ms



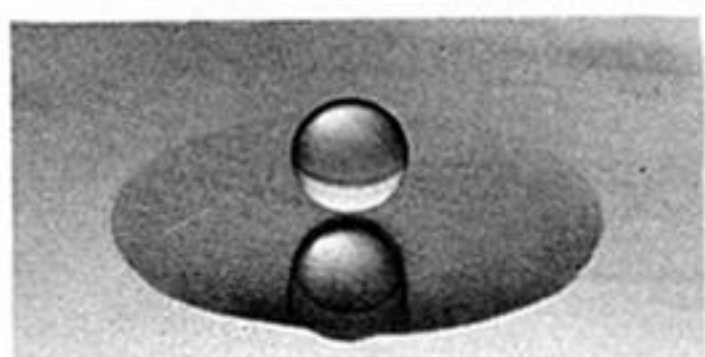
0.3 ms



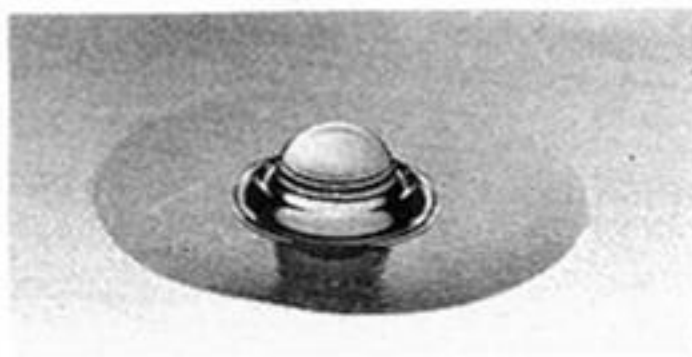
0.7 ms

0 3 mm

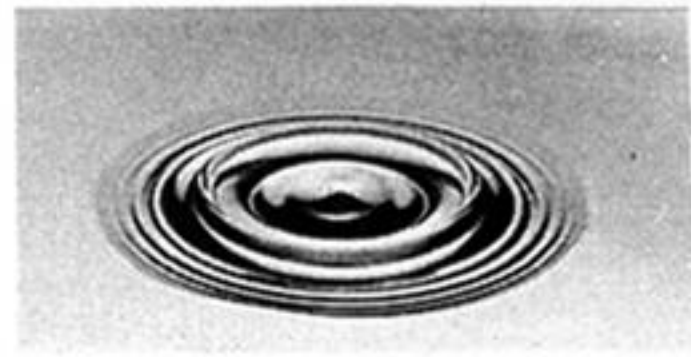
Figure 3. The impact of a n-heptane droplet on a stainless steel surface at 24 °C ($\alpha = 60^\circ$). A bubble can be seen to form at the point of impact.



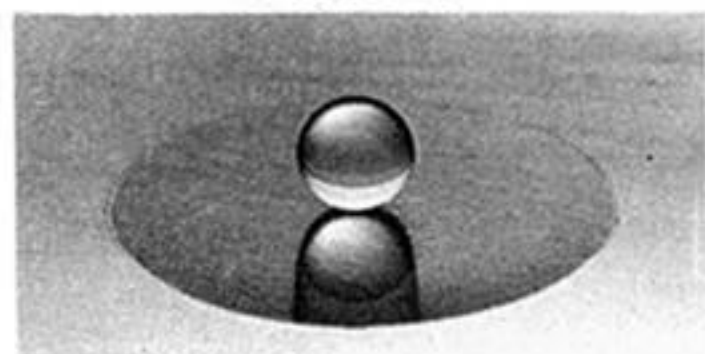
-0.1 ms



0.6 ms



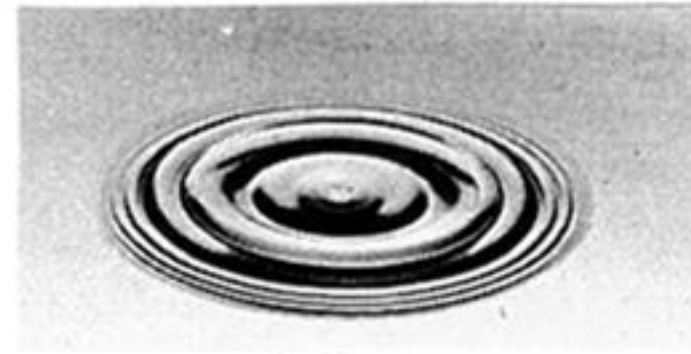
1.9 ms



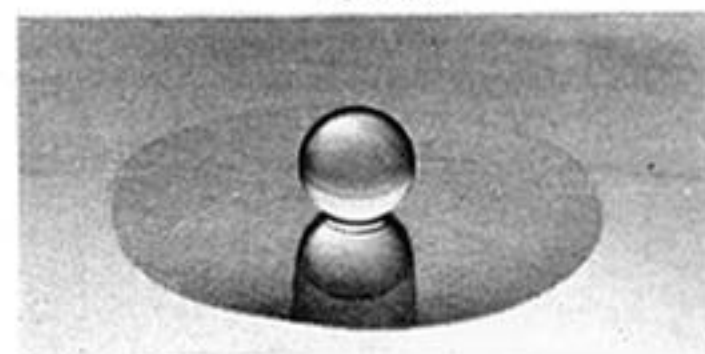
0 ms



0.7 ms



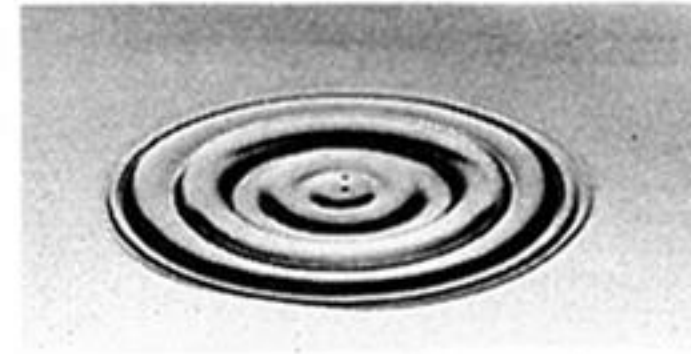
2.3 ms



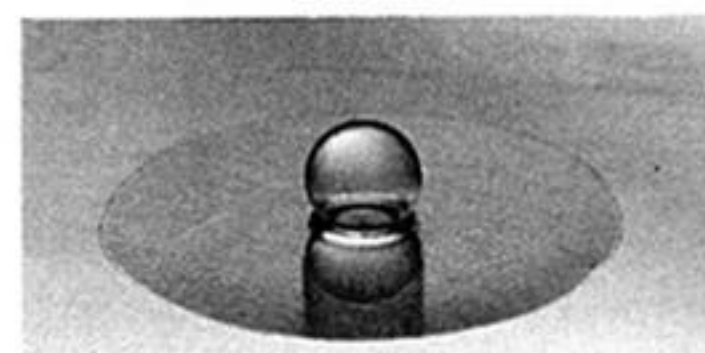
0.1 ms



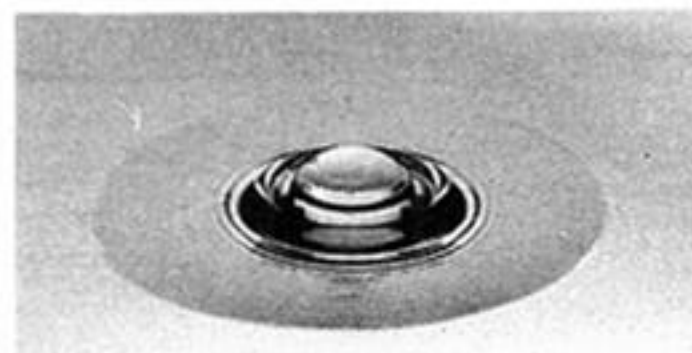
0.8 ms



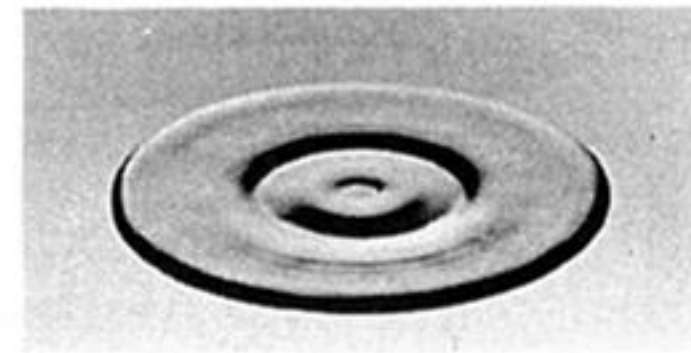
2.7 ms



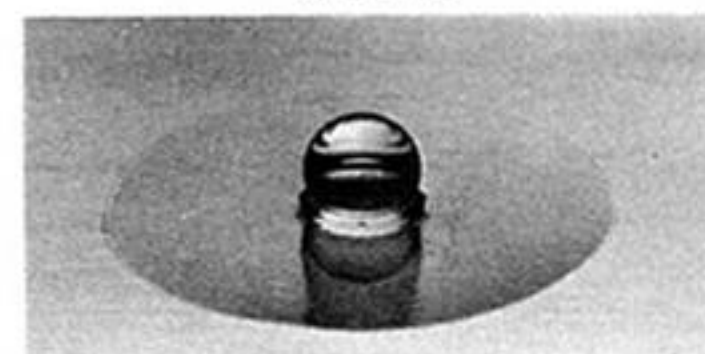
0.2 ms



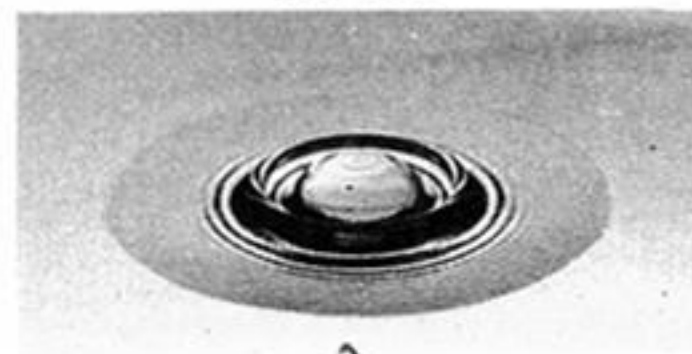
0.9 ms



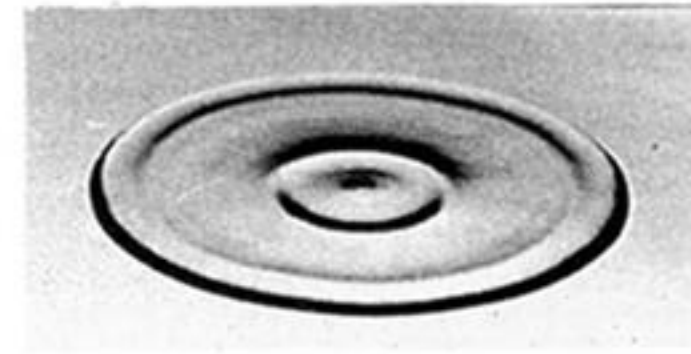
3.4 ms



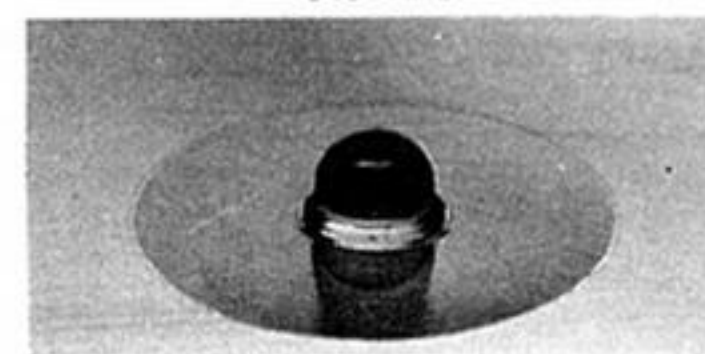
0.3 ms



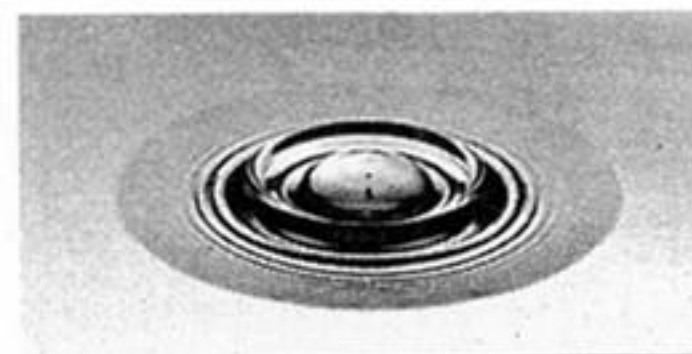
1.1 ms



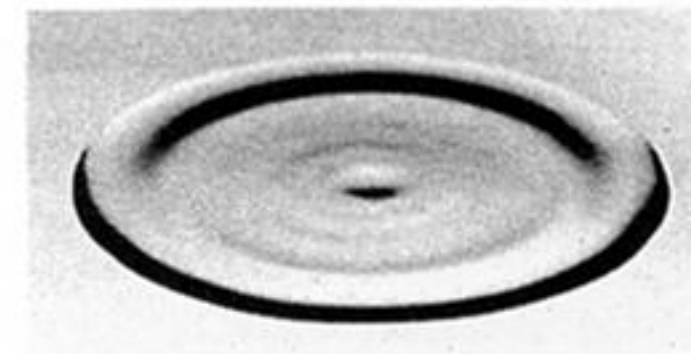
4.4 ms



0.4 ms



1.3 ms



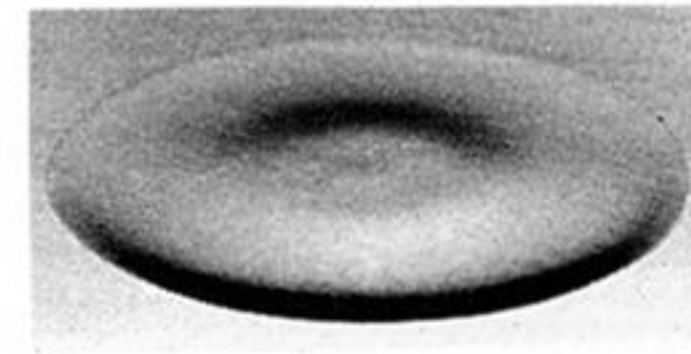
6.9 ms



0.5 ms



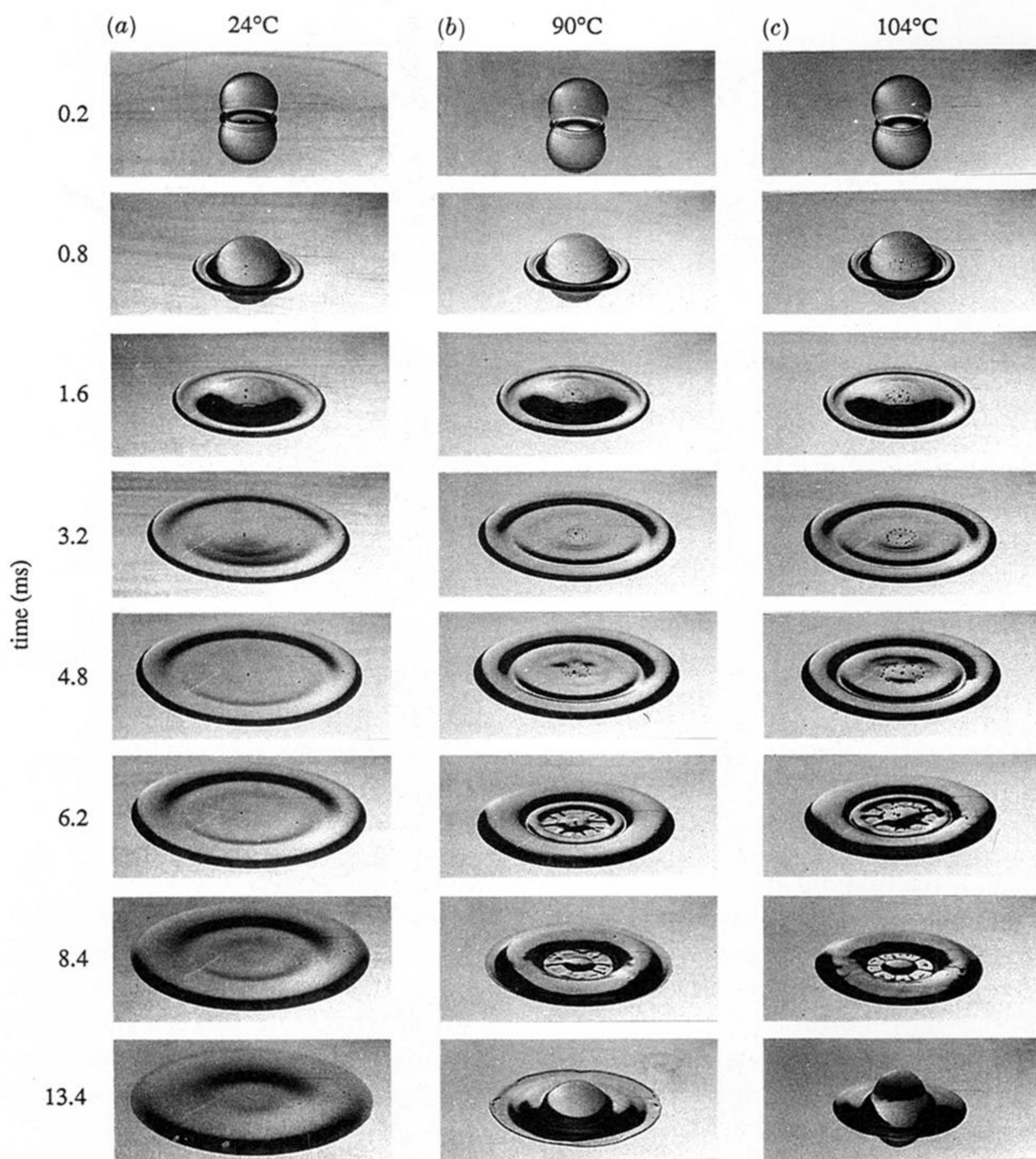
1.5 ms



19.9 ms

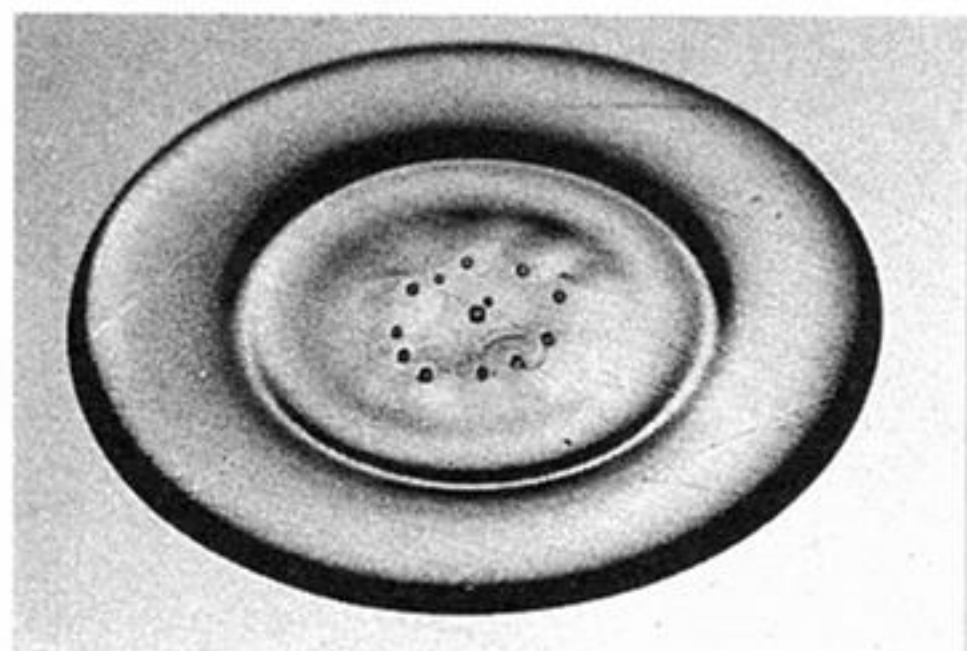
0 3 mm

Figure 4. The impact of a n-heptane droplet on a thin liquid film on a stainless steel surface at 22 °C ($\alpha = 30^\circ$).

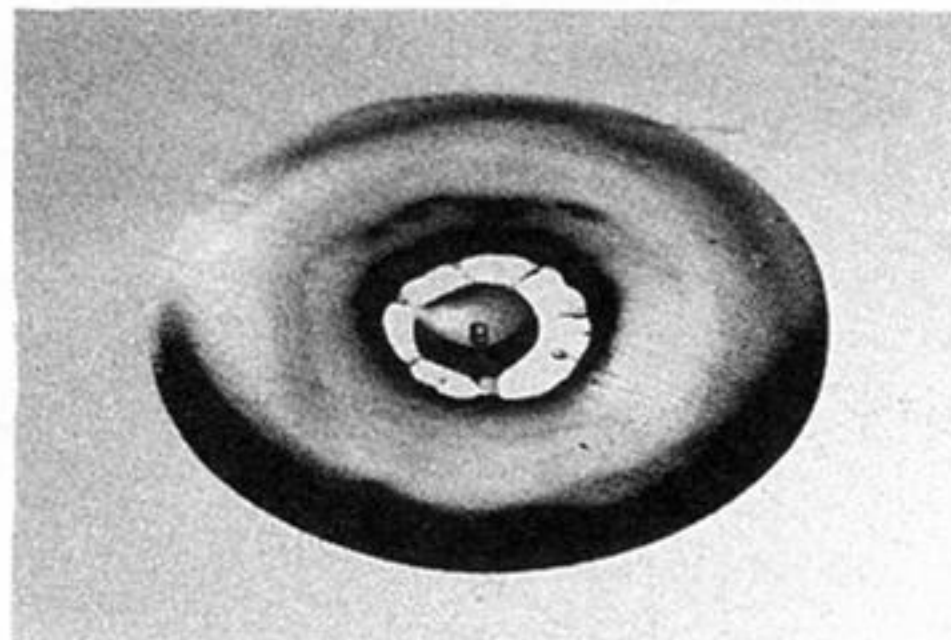


0 3 mm

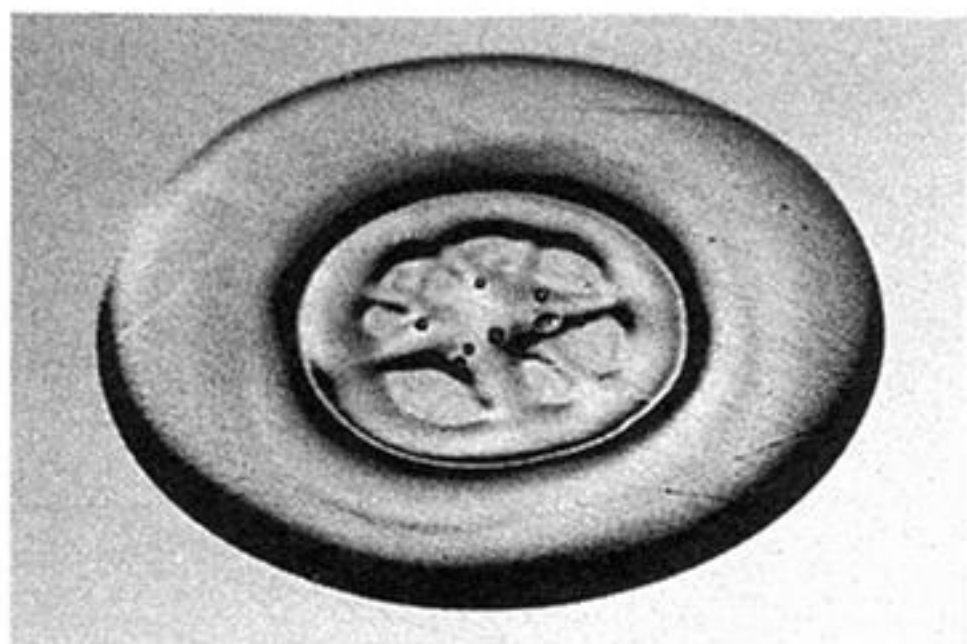
Figure 6. The impact of a n-heptane droplet on a heated stainless steel surface ($\alpha = 30^\circ$), with
 (a) $T_w = 24^\circ\text{C}$, (b) $T_w = 90^\circ\text{C}$, and (c) $T_w = 104^\circ\text{C}$.



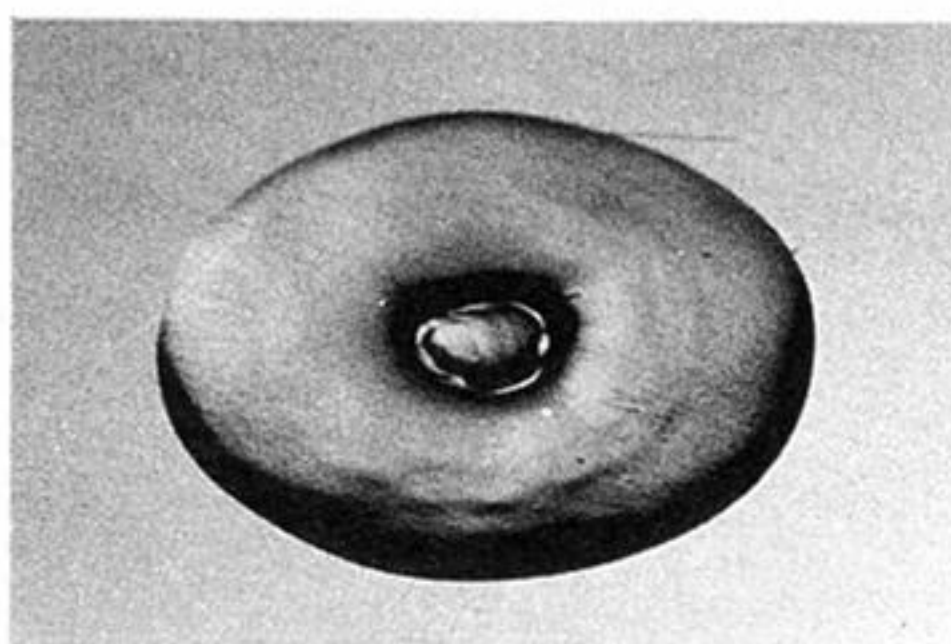
5.6 ms



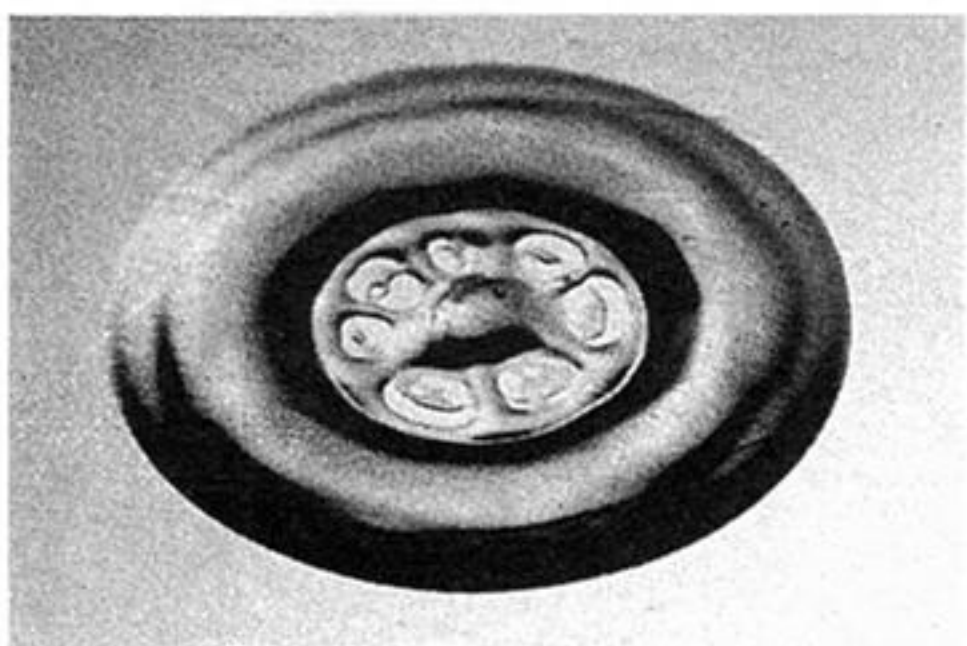
8.8 ms



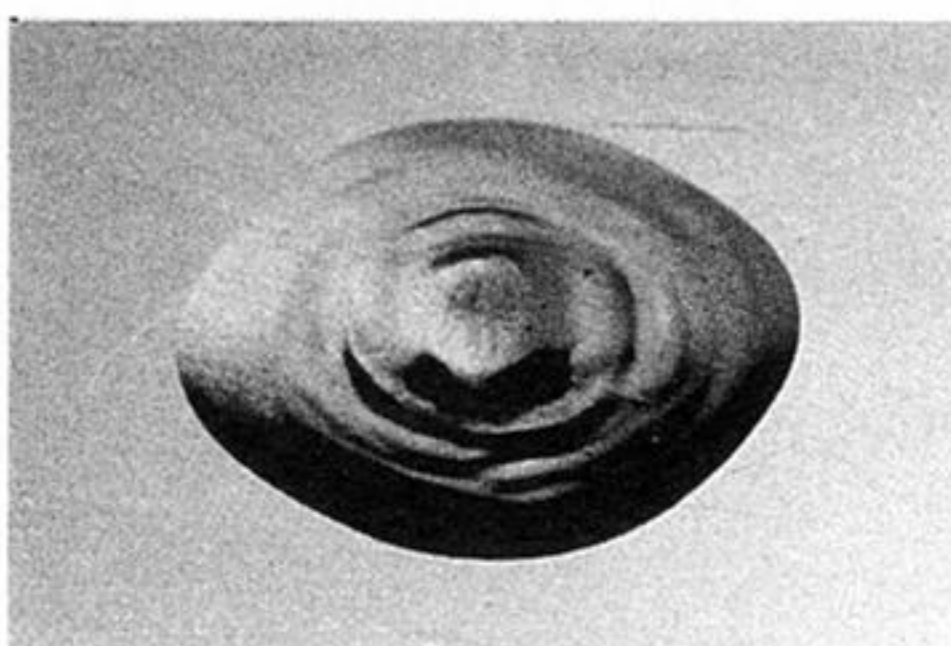
6.4 ms



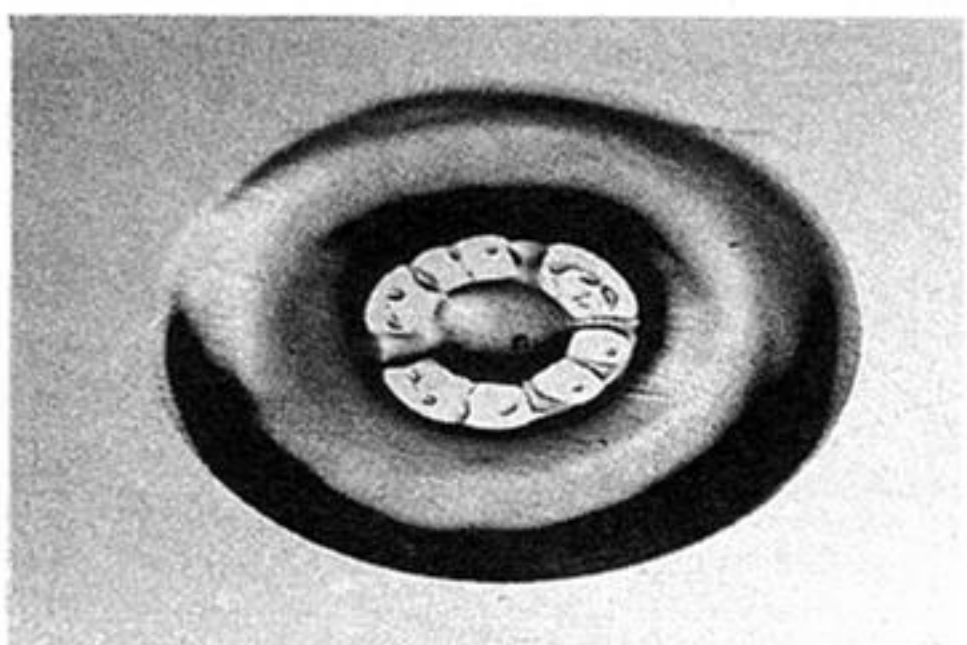
9.6 ms



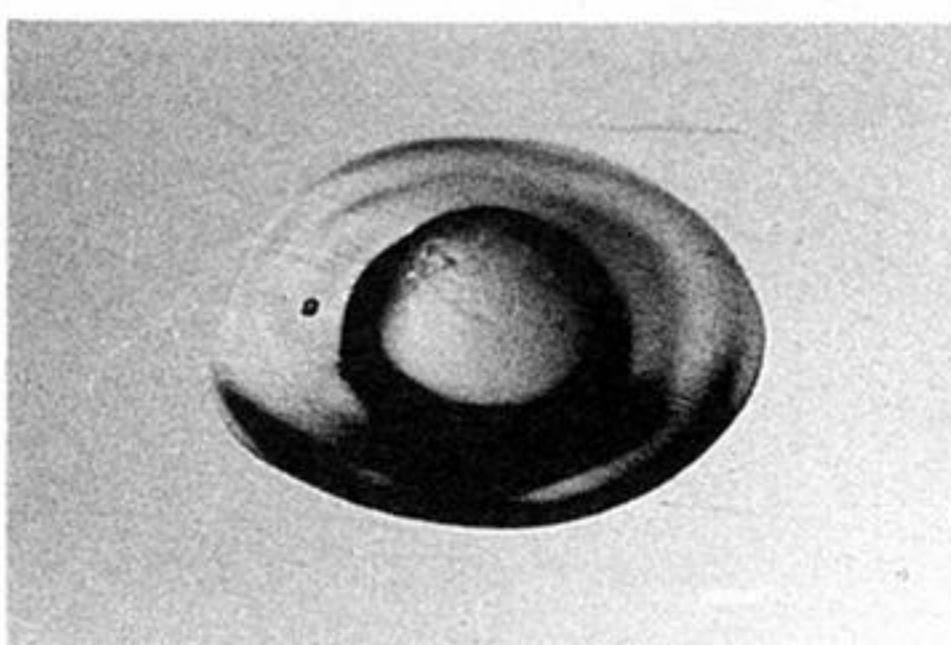
7.2 ms



11.2 ms



8.0 ms



12.8 ms

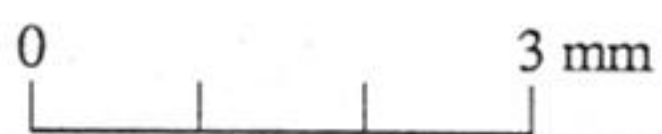
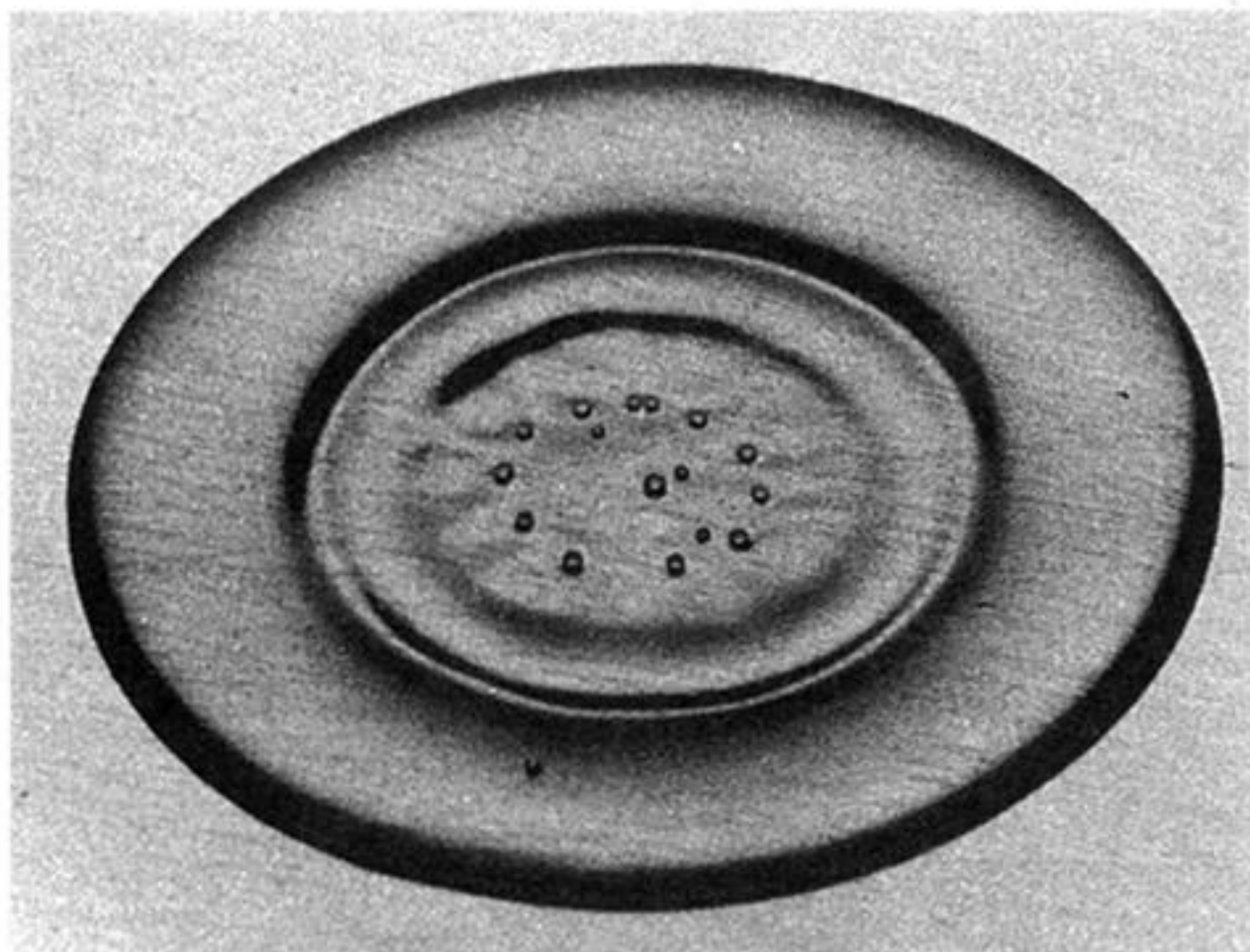
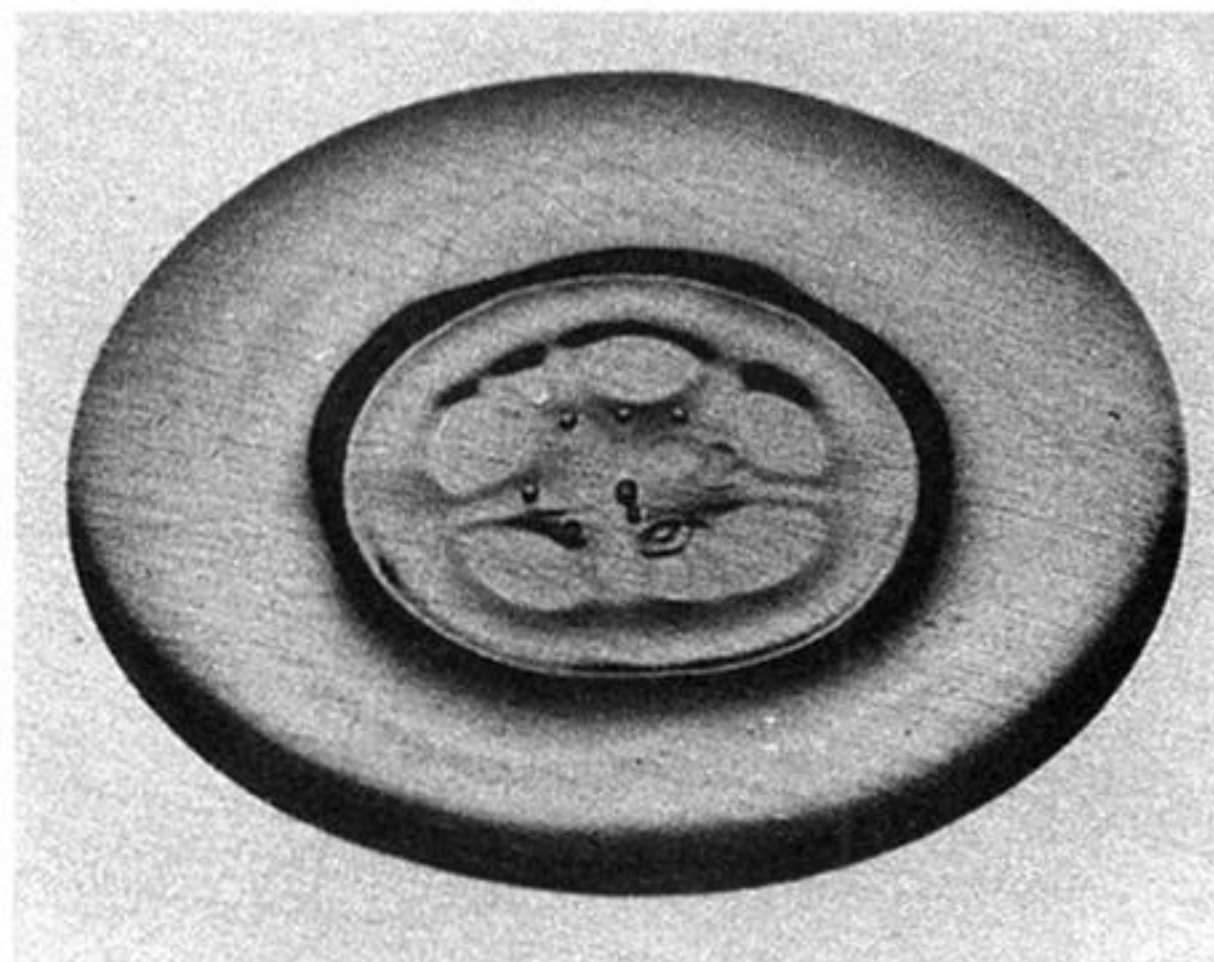


Figure 7. The formation of cellular structures in the liquid film during the spreading of a n-heptane droplet on a stainless steel surface at 104 °C ($\alpha = 60^\circ$).

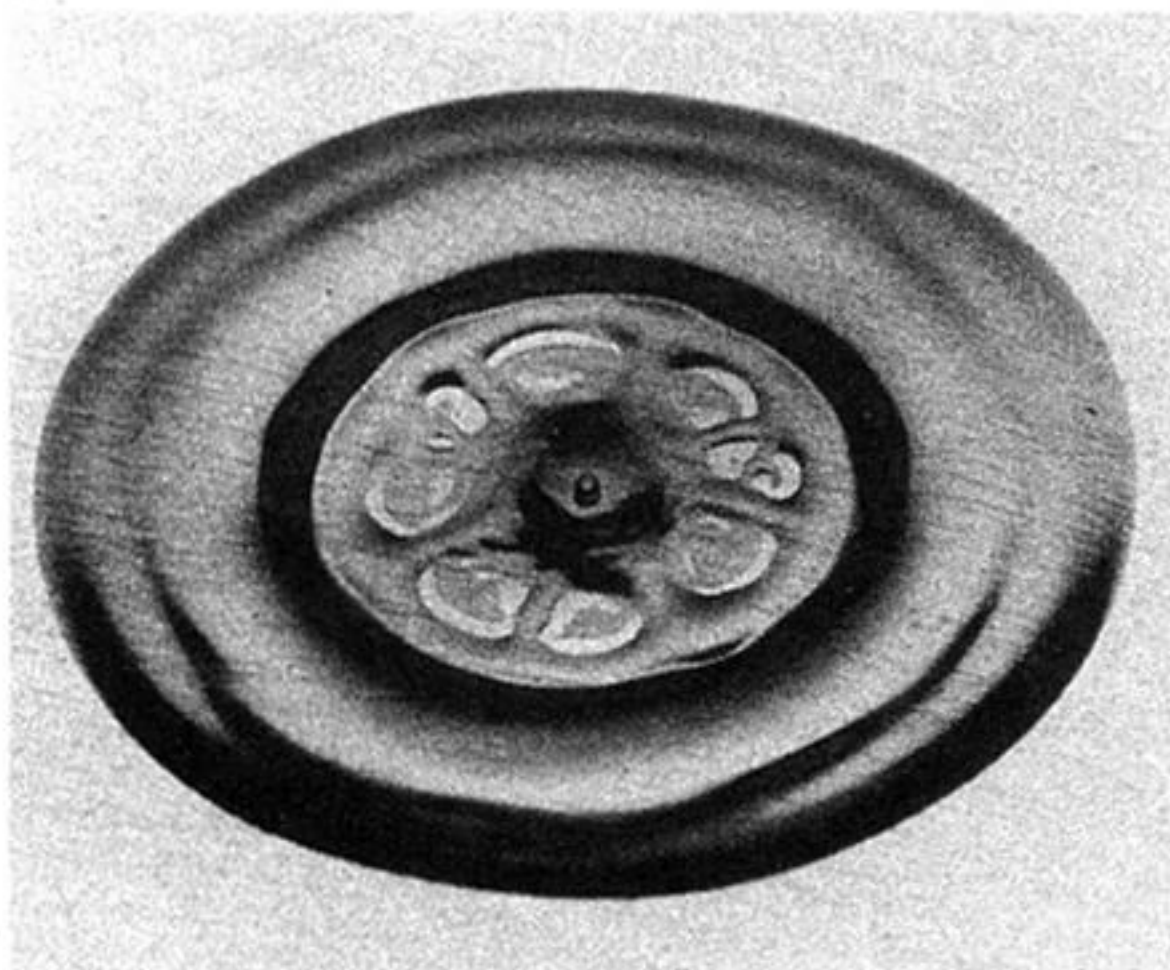
(a)



(b)



(c)



(d)

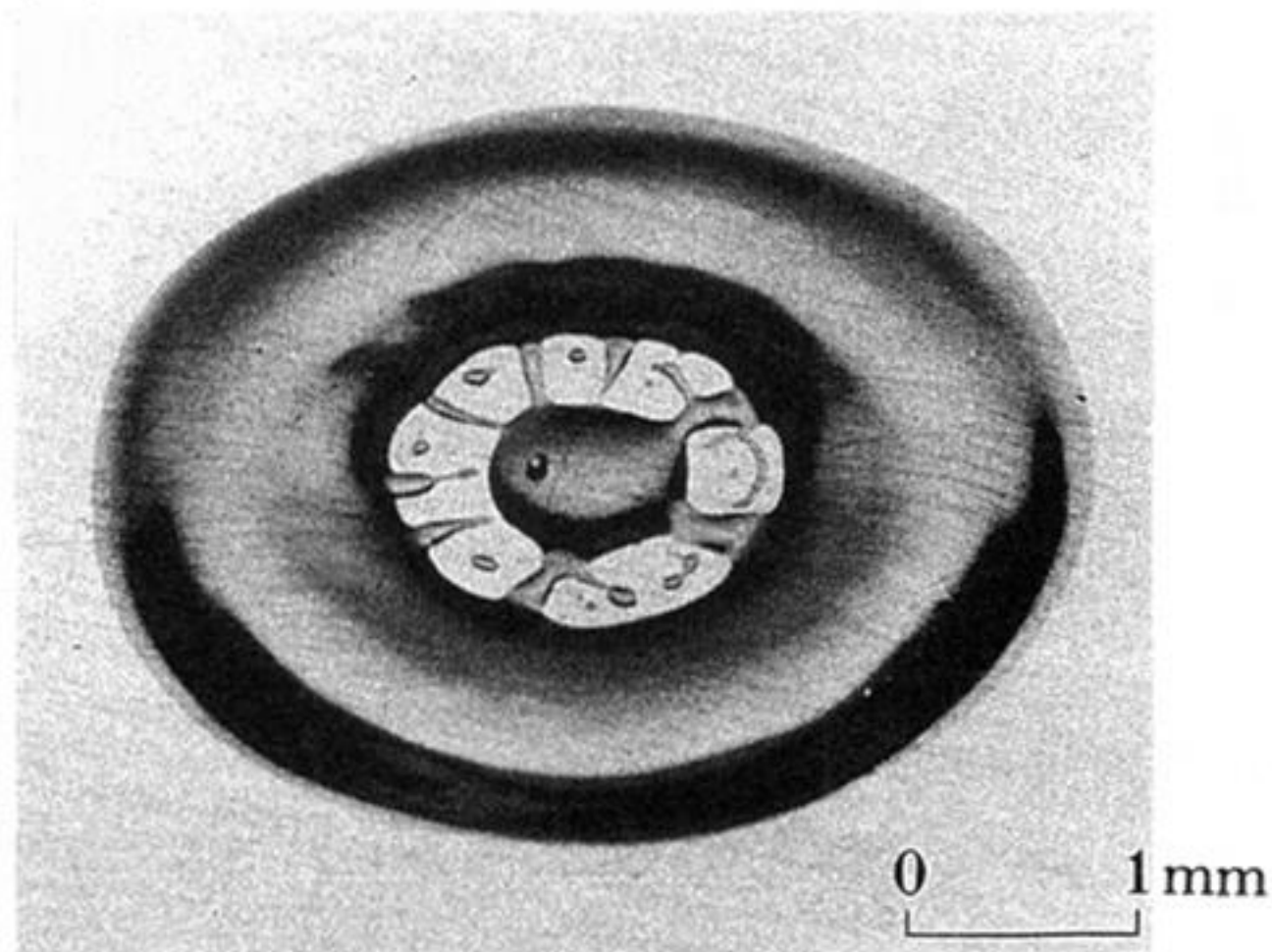


Figure 8. The impact of a n-heptane droplet on a stainless steel surface at 104 °C ($\alpha = 60^\circ$) showing (a) the formation of a bubble ring at $t = 5.6$ ms, (b) ridges on the liquid film at $t = 6.4$ ms, (c) cellular structures in the liquid film at $t = 7.2$ ms, and (d) evaporation of the liquid in the cellular structures at $t = 8.0$ ms.

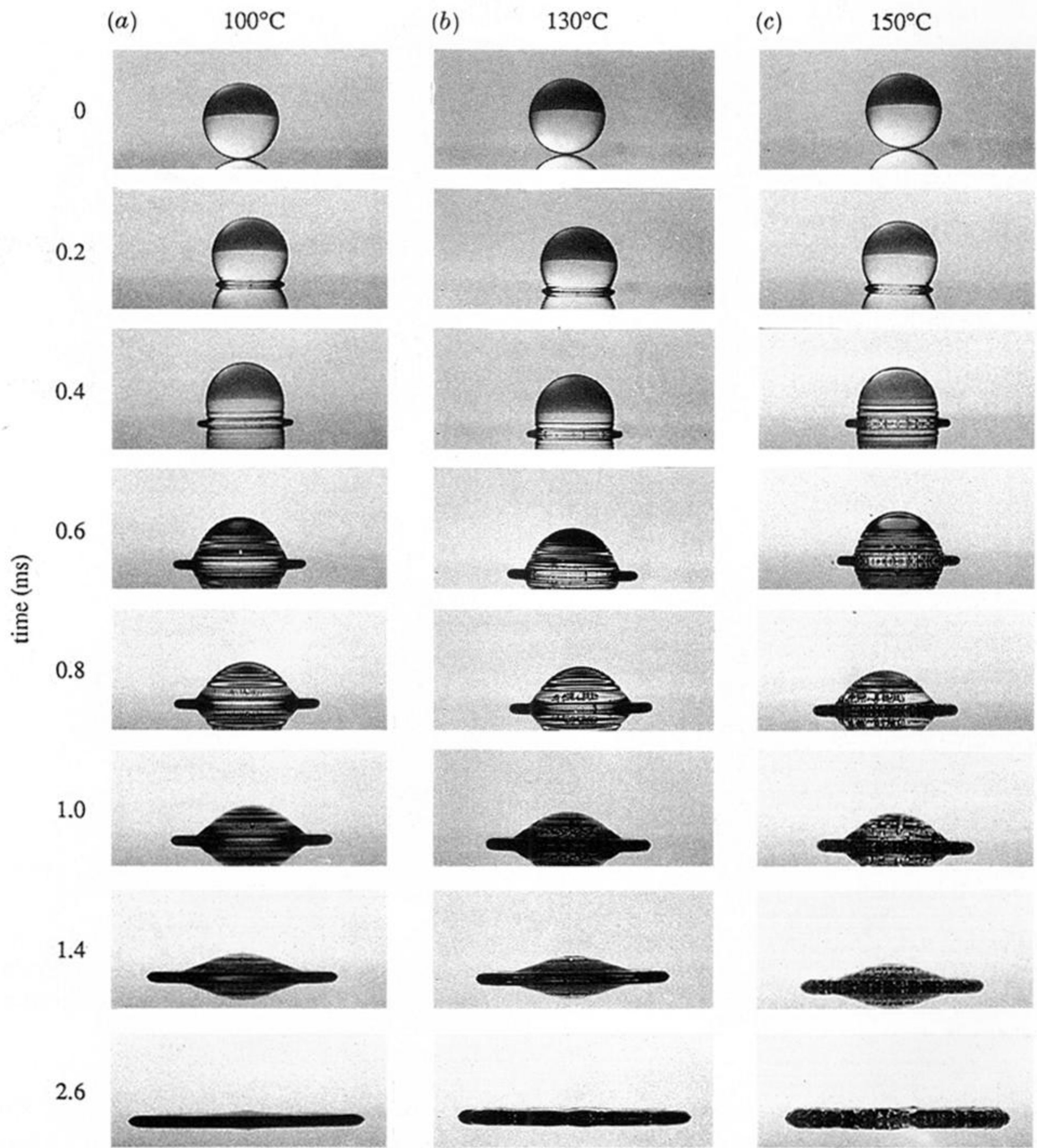


Figure 9. The impact on a n-heptane droplet on a heated stainless steel surface above the boiling point (98.4°C) of the liquid ($\alpha = 0^\circ$), (a) $T_w = 100^\circ\text{C}$, (b) $T_w = 130^\circ\text{C}$, and (c) $T_w = 150^\circ\text{C}$.

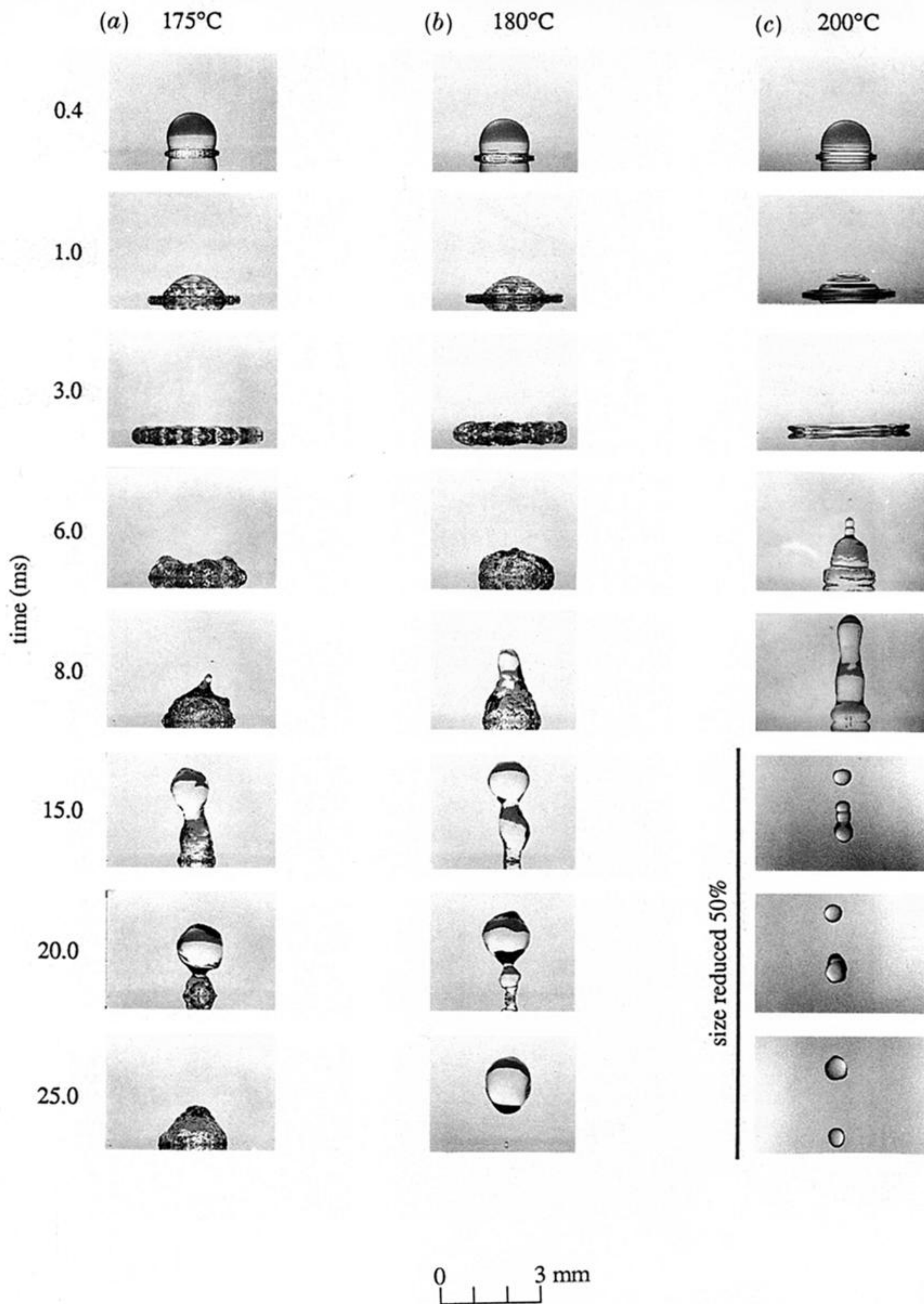


Figure 10. The transition from nucleate boiling to film boiling as T_w is raised above the Leidenfrost temperature (200 °C) of n-heptane ($\alpha = 0^\circ$) (a) $T_w = 175$ °C, (b) $T_w = 180$ °C, and (c) $T_w = 200$ °C.

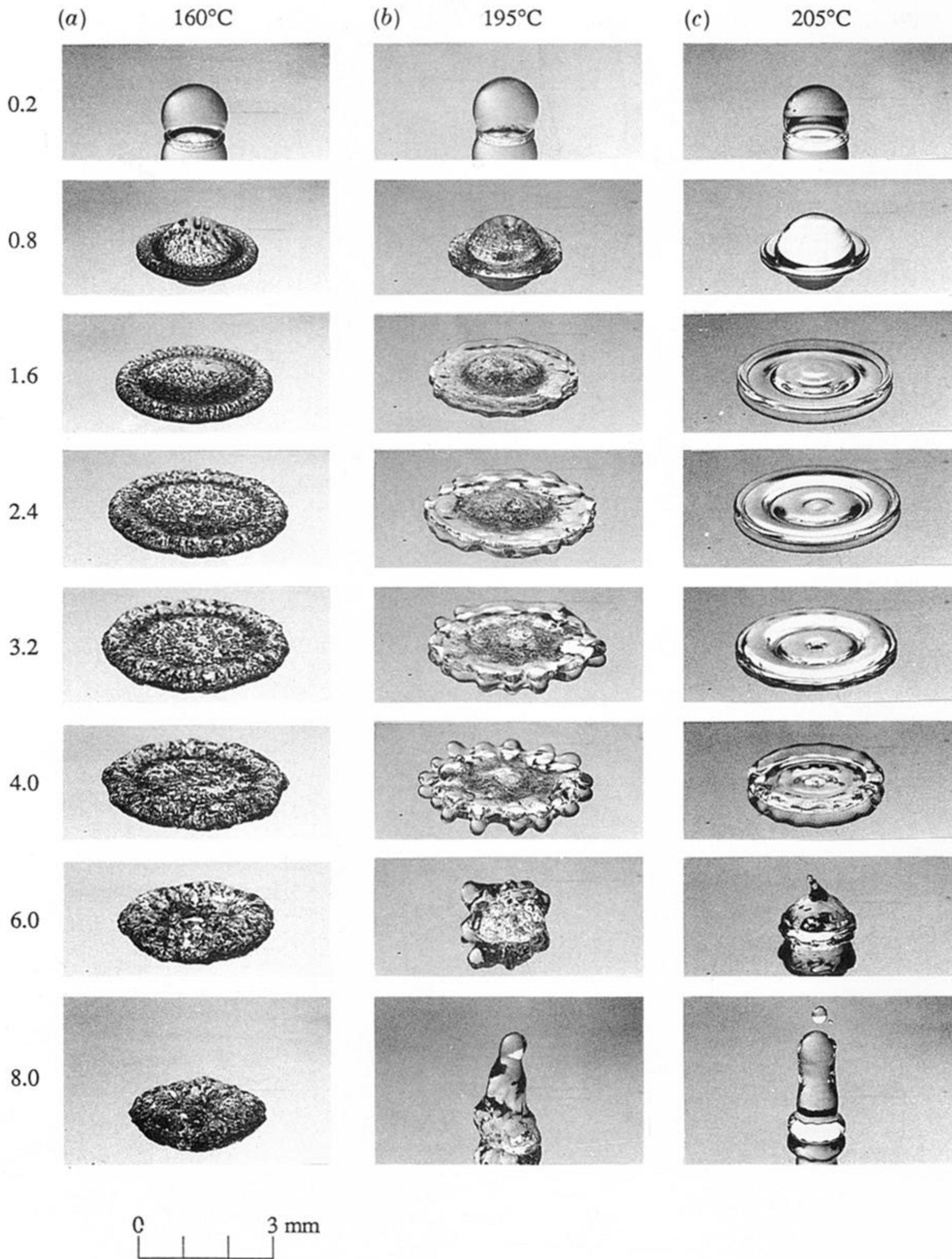
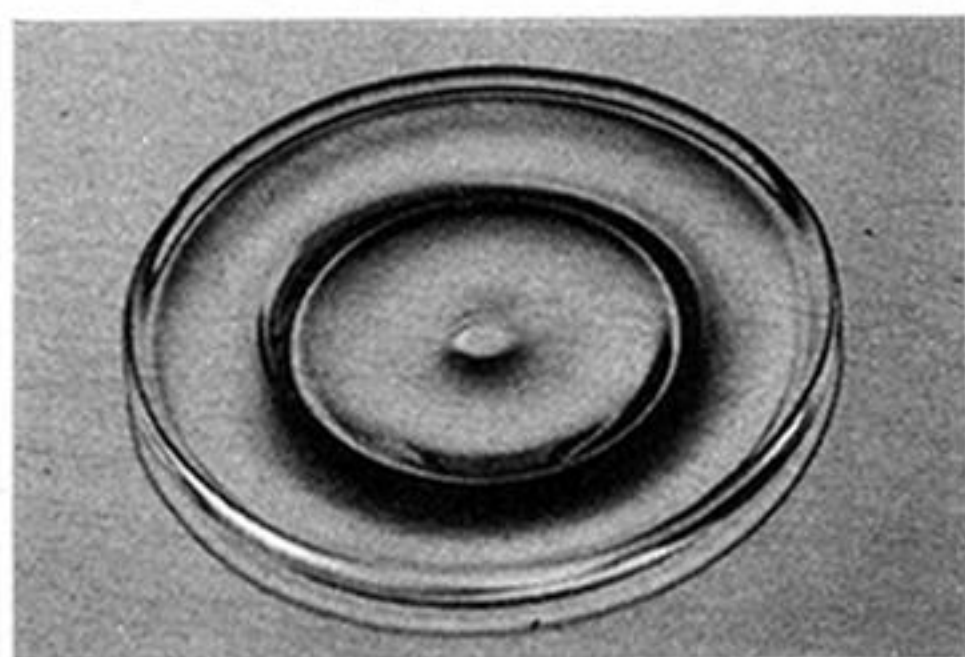


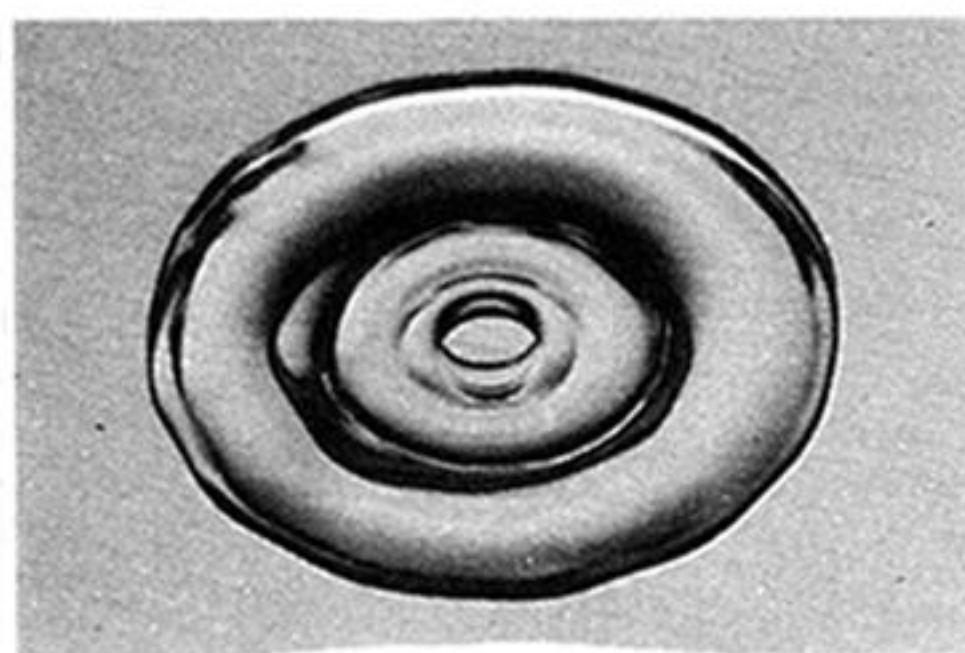
Figure 11. Additional views of the transition from nucleate boiling to film boiling ($\alpha = 30^\circ$)
 (a) $T_w = 160^\circ\text{C}$, (b) $T_w = 195^\circ\text{C}$, and (c) $T_w = 205^\circ\text{C}$.



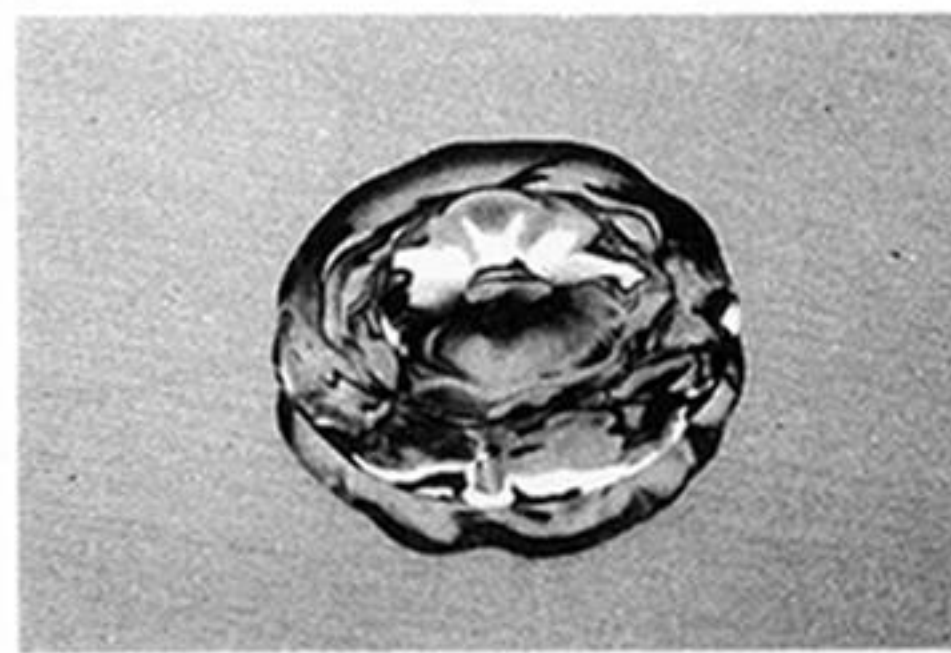
3.0 ms



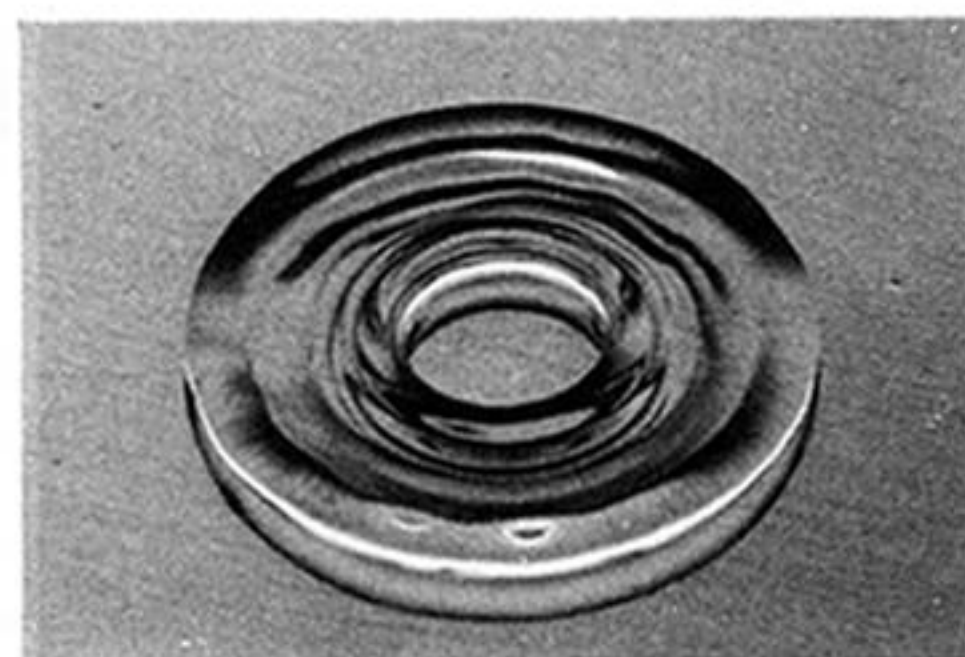
4.6 ms



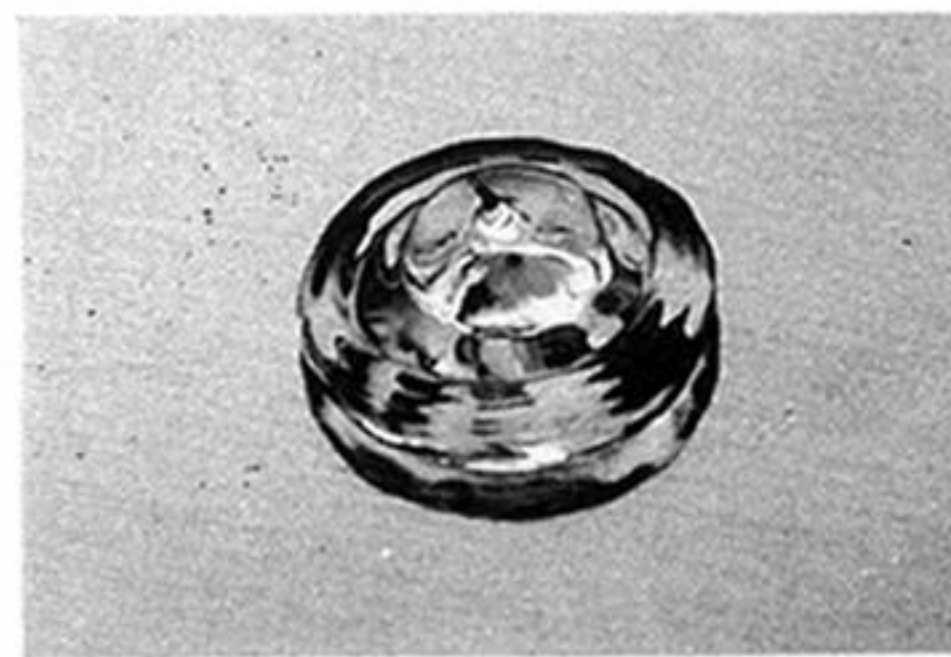
3.4 ms



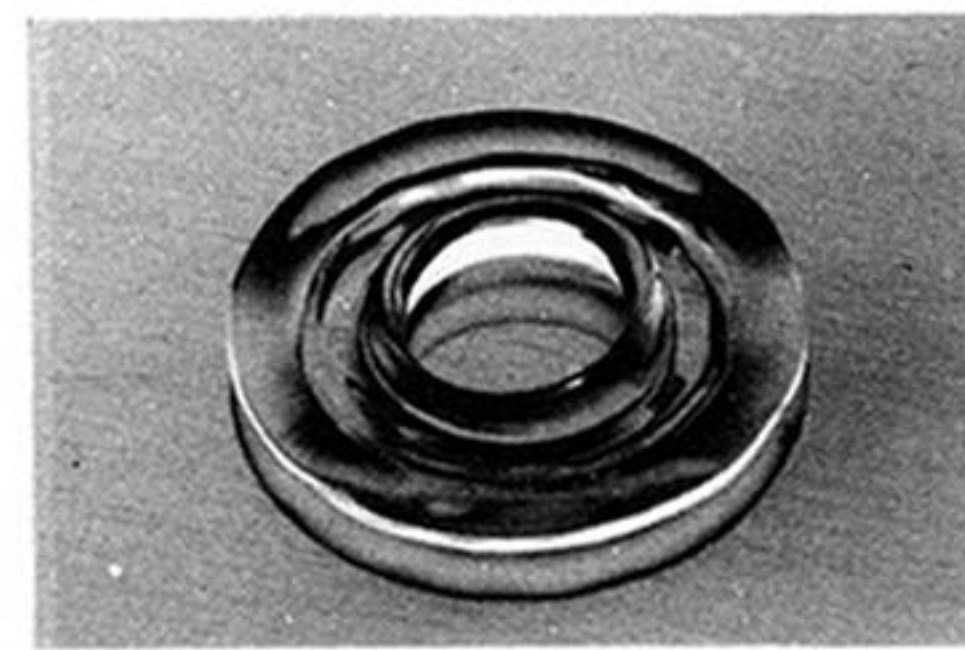
5.0 ms



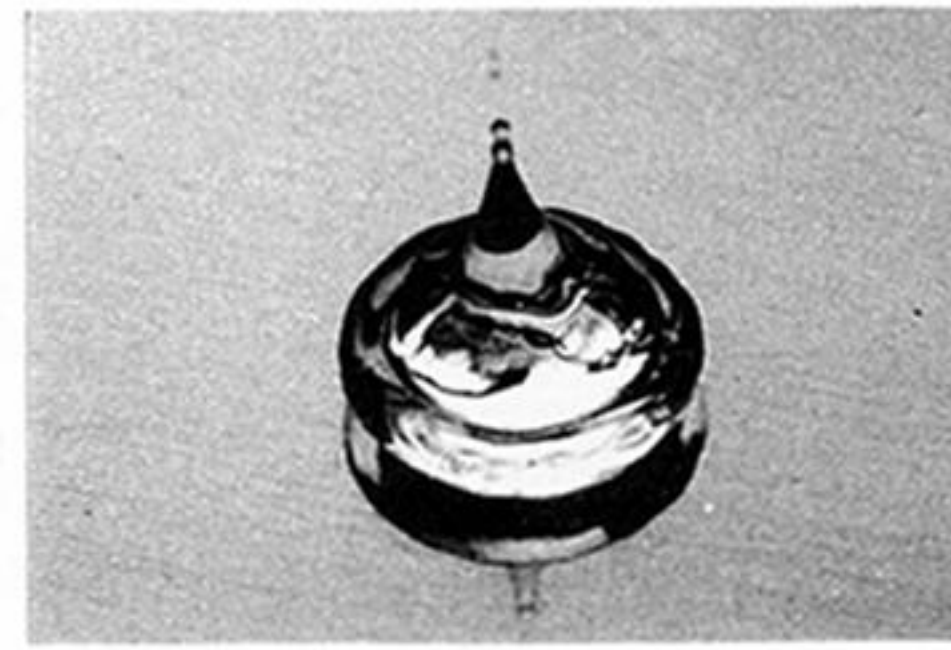
3.8 ms



5.4 ms



4.2 ms



5.8 ms

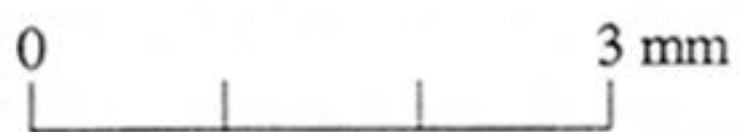
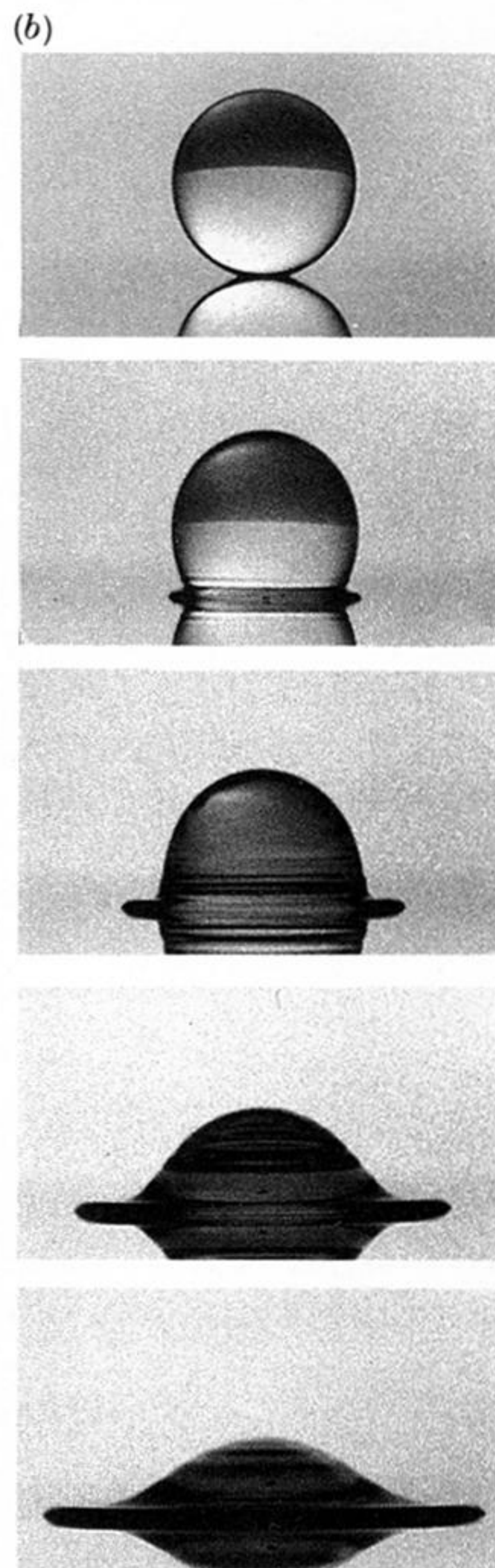
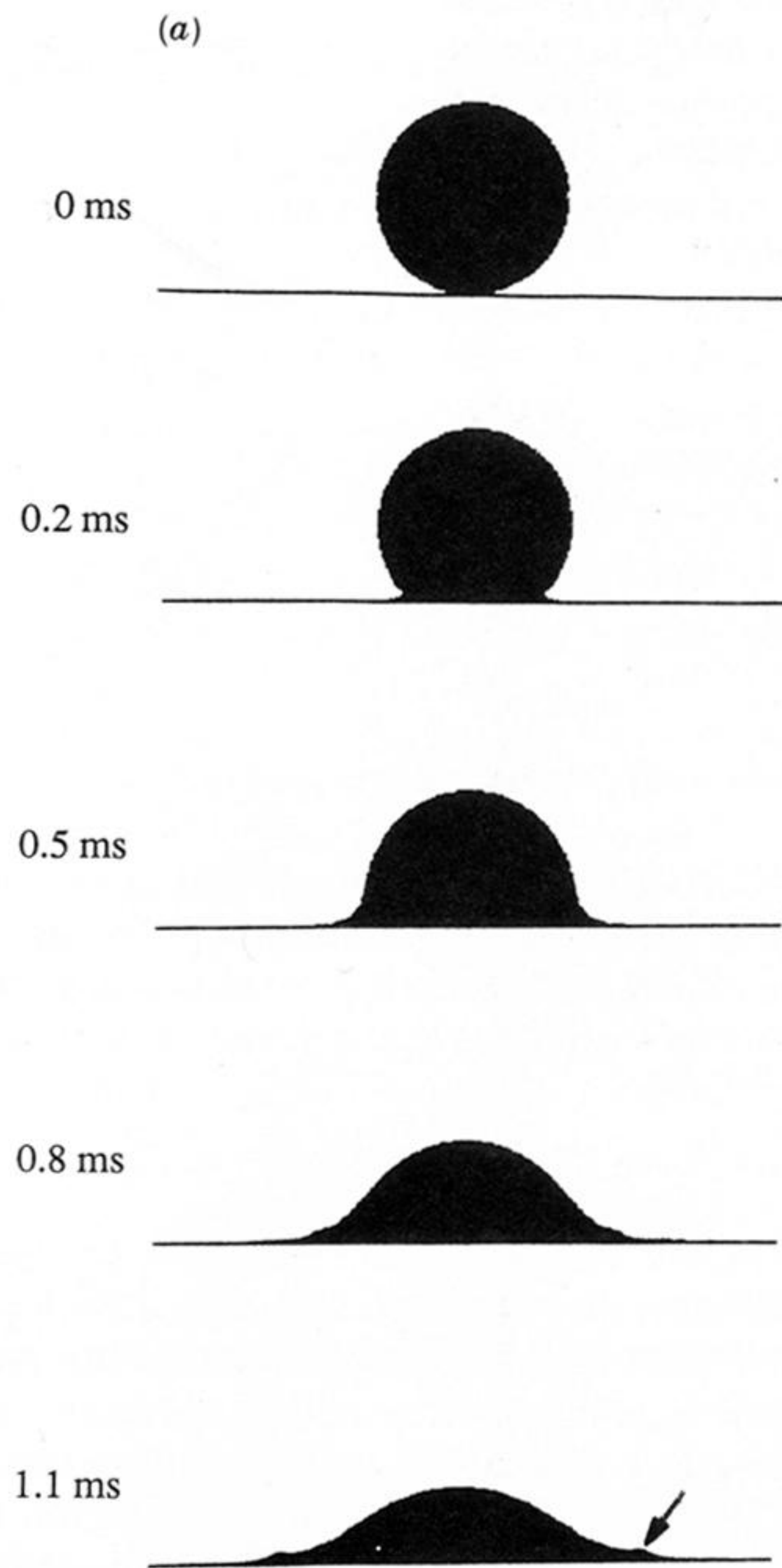


Figure 12. The formation of a hole in the centre of the liquid film during the spreading of a drop on a surface at 205 °C ($\alpha = 60^\circ$).



0 3 mm

Figure 14. Comparison of (a) the results from the model of Harlow & Shannon (1967) with (b) experimental observations from the present study of the evolution of droplet shape during the impact of a droplet on a surface at 24 °C.

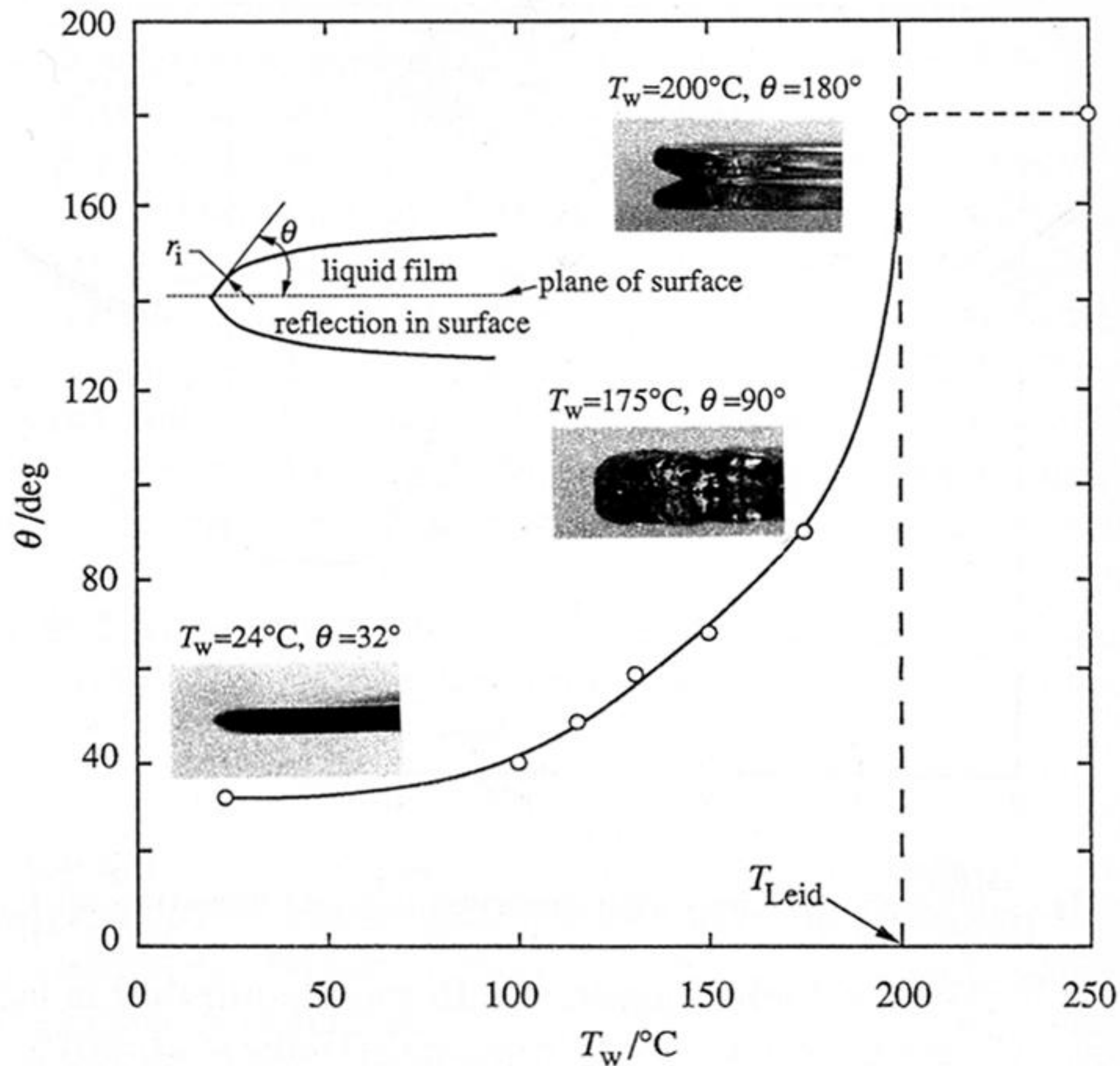


Figure 18. Variation of θ with T_w . The insets show photographs of the tip of the spreading liquid film, from which measurements of θ were made.